

Università degli Studi di Padova

Dipartimento di Fisica e Astronomia “Galileo Galilei”

TESI DI LAUREA MAGISTRALE IN FISICA

Search for Lorentz and CPT symmetries violation in double-beta decay using data from the GERDA experiment

Candidato

LUIGI PERTOLDI
MAT. 1128283

Relatore

RICCARDO BRUGNERA

Correlatore

KATHARINA CÄCILE
VON STURM ZU VEHLINGEN

Contents

Introduction	3
1 The double-beta decay	5
<i>The two-neutrino double-beta decay</i>	5
<i>The neutrinoless double-beta decay</i>	8
<i>The Lorentz violating two-neutrino double-beta decay</i>	9
2 The GERDA experiment	12
3 Data and simulations	20
<i>The GERDA data set</i>	20
<i>Monte Carlo simulations</i>	22
4 Statistical analysis	31
<i>A Bayesian approach</i>	31
<i>Background decomposition</i>	35
5 Results	38
<i>Standard Model double-beta decay mode</i>	39
<i>Lorentz-violating double-beta decay mode</i>	45
References	64

Introduction

The initial purpose of unifying Special Relativity and Quantum Mechanics has led to the establishment of one of the building blocks of the theory behind the Standard Model: its invariance with respect to linear transformations of space-time, the so-called Lorentz transformations. Lorentz was one of the first to study the invariance laws of Maxwell's equations and some years later Einstein showed that these transformations were a natural consequence of the foundations of Special Relativity, namely the constantness of the speed of light in every inertial frame of reference. However, recent research activities in Quantum Gravity show that this symmetry is in fact nothing sacred, and its breakdown at the Planck scale cannot be excluded. Lorentz symmetry is also strongly tied to CPT symmetry (the combination of Charge, Parity and Time-reversal transformations) by the CPT theorem. This theorem states that every local, relativistic quantum field theory must be CPT invariant.

The neutrino is playing the role of a messenger of the new Physics beyond the Standard Model. Studying the properties and interactions of neutrinos has been one of the most exciting and vigorous activities in Particle Physics and Astrophysics ever since Pauli first proposed their existence in 1930. In spite of their weakly interacting nature, we have so far accumulated an enormous amount of knowledge about them. No experiments that have been performed so far have detected conclusive deviations from the Standard Model, except neutrino oscillation experiments, which have shown that neutrinos are massive and mixed. The understanding of how the neutrinos would gain tiny masses and how they are mixed is an extremely challenging task that we have to face. The consequences could make the Standard Model an effective theory of the yet unknown theory beyond it.

An open question of fundamental importance concerns the nature of these particles, which could be either of Dirac or Majorana type (i.e. neutrino and anti-neutrino are distinct particles or the same particle). An attempt to address this problem is done by experiments looking for the neutrinoless mode of double-beta decay. The double-beta decay, in its two-neutrino Standard Model mode ($2\nu\beta\beta$), consists in a nucleus that decays into a daughter nucleus with two electrons and two electron-anti-neutrinos as a byproduct. If the neutrino is a Majorana particle then another mode may occur ($0\nu\beta\beta$), in which neutrinos are not produced at all. Neutrinoless double-beta decay experiments are considered the most promising way to solve the enigma, although these events are very rare processes controlled by weak interactions. One of these is the GERDA experiment, located at LNGS in Italy at a depth of 3500 m w.e. (water equivalent). GERDA submerses bare high-purity germanium detectors enriched in ^{76}Ge into liquid argon (LAr), which serves simultaneously as a shield against external radioactivity and as a cooling medium, in order to substantially reduce background events. In these types of experiments the source is equal to the detector which yields high detection efficiency, allowing to reach a superior energy resolution and enhance the ability to discriminate background from signal.

A careful study of the two-neutrino double-beta decay is also performed by these experiments. The high precision that many of them have reached has motivated the

formulation of different modes of double-beta decay so that experiments can also look for new Physics through unconventional decay modes. As quoted above, the spontaneous breakdown of the Lorentz symmetry is an interesting feature that can be accommodated by many candidate theories of Quantum Gravity, such as String Theory. The general framework that incorporates operators that break Lorentz invariance in the Standard Model is the Standard Model Extension. This effective field theory parametrizes generic deviations from Lorentz invariance in the form of coordinate-invariant terms in the action by contracting operators of conventional fields with controlling coefficients for Lorentz violation. It should be noted that a subset of operators in the Standard Model Extension also breaks CPT symmetry. All quantum field operators for Lorentz violation involved in the propagation of neutrinos have been classified and enumerated. Their effects show up in neutrino oscillations experiments and time-of-flight experiments. However, four operators, odd under CPT, cannot be detected in this way, instead, they must be accessed through physical processes that involve neutrino phase-space properties, such as particle decays. The net effect on the energy spectrum of the decay products is a distortion regulated by a combination of the four operators' coefficients, denoted with $\dot{a}_{\text{of}}^{(3)}$.

In this work we study the summed energy spectrum of the electrons produced in $2\nu\beta\beta$ detected by the GERDA experiment, in order to extract an upper limit for $\dot{a}_{\text{of}}^{(3)}$. In order to accomplish this, background modeling is an essential step: starting from the screening measurements of the radioactivity inside GERDA's components, energy spectra of various background sources are simulated inside the apparatus taking its geometry into account. Then, the presence of the isotopes is tested by fitting the simulated spectra of different contributions to the measured energy spectrum with a Bayesian statistical analysis. Data from the screening measurements of the GERDA components are used to set prior distributions on the activities of the background sources, and a p-value is used to provide a goodness-of-fit criterion. The presence of all the hypothetical contaminations is tested in a maximal model that contains all possible contributions; then a minimal model is built ruling out step-by-step the sources indicated as possibly absent by the fitting procedure. The Background Index (BI), namely the number of counts over units of energy, mass and time in the Region of Interest (RoI) around the Q-value of $2\nu\beta\beta$, is estimated for all the background contributions. With this minimal background model, the half-life of $2\nu\beta\beta$ is extracted only considering the Standard Model contribution, then the CPT-violating mode is included, and an upper limit on $\dot{a}_{\text{of}}^{(3)}$ computed.

In §1 all the theoretical notions that underlie the phenomenon under study are detailed, then a description of the GERDA experimental setup is given in §2. We provide a description of the data sets and the Monte Carlo simulations in §3 and a description of the statistical methodology in §4. Finally, the results of the analysis are presented in §5.

1 The double-beta decay

In this section we briefly review the theory of double-beta decay in its two most studied modes, the two-neutrino and the neutrinoless one, together with the mode which is relevant to this work, the Lorentz-violating one. We calculate the differential decay rates associated to the two-neutrino and the Lorentz-violating modes that will be cited in the following sections. Finally the current experimental knowledge about the Lorentz-violating mode is presented.

The two-neutrino double-beta decay

The two-neutrino double-beta decay ($2\nu\beta\beta$) processes, first suggested by M. Goeppert-Mayer in 1935 [1], can be schematically defined as:

$$\begin{aligned} \mathcal{N}(A, Z) &\longrightarrow \mathcal{N}(A, Z + 2) + 2e^- + 2\bar{\nu}_e & [2\nu\beta^-\beta^-] \\ \mathcal{N}(A, Z) &\longrightarrow \mathcal{N}(A, Z - 2) + 2e^+ + 2\nu_e & [2\nu\beta^+\beta^+] \end{aligned},$$

where $\mathcal{N}(A, Z)$ represents a nucleus with mass number A and atomic number Z . A $2\nu\beta^-\beta^-$ ($2\nu\beta^+\beta^+$) process consists of the simultaneous β^- (β^+) decay of two neutrons (protons) in the same nucleus. The processes are generated at second-order in the perturbative expansion of weak interactions in the Standard Model. The Feynman graph for $2\nu\beta^-\beta^-$ is shown in Fig. 1, left.

Since the $2\nu\beta\beta$ decays have a four-body leptonic final state, the sum of the kinetic energies of the two decay electrons have a continuous spectrum from zero to the Q-value of the decay process (the recoil energy of the final nucleus is negligible), which is given by

$$Q_{\beta\beta} = M_i - M_f - 2m_e, \quad (1)$$

where M_i and M_f are, respectively, the masses of the initial and final nuclei (i.e. the energy levels of their ground states; if the transition occurs into an excited energy level of the final nucleus, M_f must be replaced with the appropriate energy).

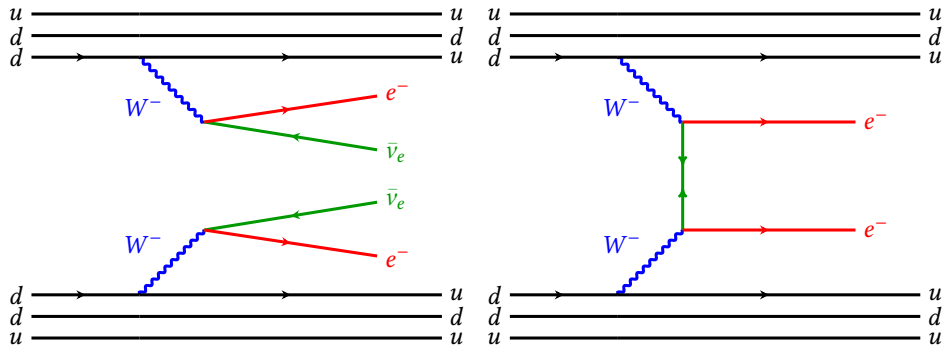


Figure 1: Feynman graphs for two-neutrino (left) and neutrinoless (right) double-beta decay.

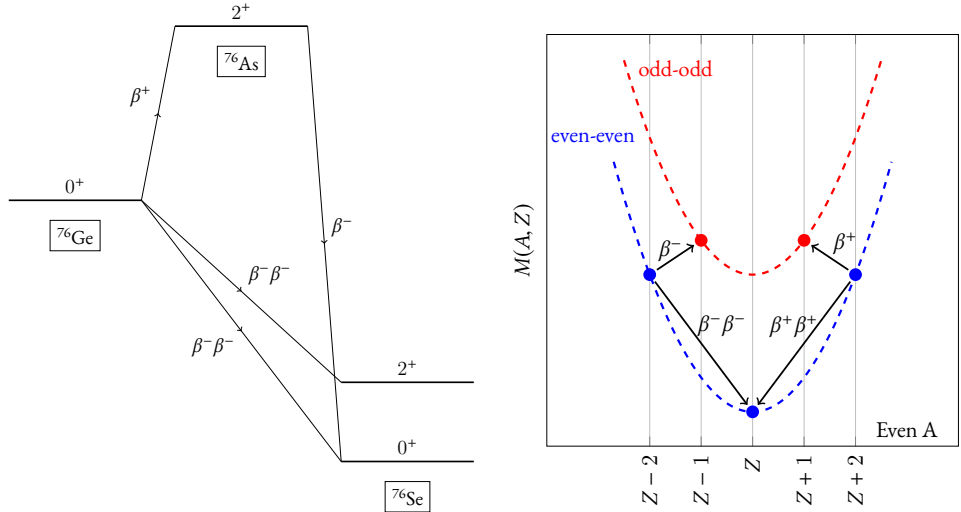


Figure 2: On the left: schematic illustration of the energy level structure of the $2\nu\beta^-\beta^-$ decay of ^{76}Ge into ^{76}Se . On the right: general energy level configuration for double-beta decay emitters. The situation for a nucleus with even mass number A is presented: the mass parabola, representing the dependence of the binding energy $M(A, Z)$ on the atomic number Z , is plotted for even-even (even number of protons and neutrons) and odd-odd nuclei with the relevant β and $\beta\beta$ decays among them.

A nucleus $\mathcal{N}(A, Z)$ can decay through a $2\nu\beta\beta$ process if its ground state has an energy which is larger than the ground-state energy of the nucleus $\mathcal{N}(A, Z \pm 2)$ plus twice the electron mass. Moreover, if a nucleus can decay through both the β and $2\nu\beta\beta$ processes, in practice the latter is not observable, because its β decay lifetime is much shorter than its $2\nu\beta\beta$ decay lifetime (the half-life of $2\nu\beta\beta$ is typically around $10^{19} - 10^{24}$ yrs). Therefore, in practice the $2\nu\beta\beta$ decay of a nucleus is observable only if its β decay is energetically forbidden or strongly suppressed because of a large change of spin. The β^- decay of a nucleus $\mathcal{N}(A, Z)$ is energetically forbidden if its ground-state energy is lower than the ground-state energy of the nucleus $\mathcal{N}(A, Z + 1)$ plus the electron mass ($Q_{\beta^-} < 0$). Typically, in $2\nu\beta^-\beta^-$ decays the energy levels of the three nuclei $\mathcal{N}(A, Z)$, $\mathcal{N}(A, Z + 1)$, and $\mathcal{N}(A, Z + 2)$ are of the type depicted in Fig. 2, left, where the specific case of ^{76}Ge , ^{76}As , and ^{76}Se nuclei is considered.

$2\nu\beta^-\beta^-$

The naturally occurring isotopes which can decay through the $2\nu\beta^-\beta^-$ process, with forbidden or suppressed β^- decay are 35, and they are listed in [2]. All of the initial and final nuclei in the $2\nu\beta^-\beta^-$ process are even-even, i.e. they have an even number of protons and neutrons. Their binding energy is larger than the intermediate odd-odd nuclei one because of the pairing force acting between identical nucleons (see Fig. 2, right). For the same reason, all of the initial and final nuclei have a 0^+ ground state. Therefore, all ground-state to ground-state transitions are $0^+ \rightarrow 0^+$. Ground-state transitions to an excited state of the final nucleus may be energetically allowed, as in the case of the $^{76}\text{Ge} \rightarrow ^{76}\text{Se}$ decay in Fig. 2, left, in which there is an accessible 2^+ excited state of

^{76}Se . However, due to a cancellation occurring in the phase space integral and the lower Q-value [3], the $0^+ \rightarrow 2^+$ double-beta decay is suppressed with respect to $0^+ \rightarrow 0^+$.

There are only six naturally occurring isotopes which can decay through the $2\nu\beta^+\beta^+$ process [4]. These isotopes have small Q-values and lifetimes which are much longer than the lifetimes of the $2\nu\beta^-\beta^-$. The reason for the rarity of $2\nu\beta^+\beta^+$ -decaying isotopes and their small Q-values can be understood considering that the decay $\mathcal{N}(A, Z) \rightarrow \mathcal{N}(A, Z - 1)$ can occur in two ways:

$$\begin{aligned} \mathcal{N}(A, Z) &\rightarrow \mathcal{N}(A, Z - 1) + e^+ + \nu_e & [\beta^+] \\ e^- + \mathcal{N}(A, Z) &\rightarrow \mathcal{N}(A, Z - 1) + \nu_e & [\text{EC}] \end{aligned} .$$

Since $Q_{\text{EC}} = Q_{\beta^+} + 2m_e$, the electron-capture process (EC) can occur even if the β^+ process is energetically forbidden ($Q_{\beta^+} < 0$). Thus, in order to have an energetically forbidden $\mathcal{N}(A, Z) \rightarrow \mathcal{N}(A, Z - 1)$ transitions, the ground-state energy of $\mathcal{N}(A, Z)$ must be smaller than the ground-state energy of the nucleus $\mathcal{N}(A, Z - 1)$ minus the electron mass ($Q_{\text{EC}} < 0$). Considering as a reference the energy of the ground-state energy of the intermediate nucleus, the ground-state energy of the initial nucleus in a $2\nu\beta^+\beta^+$ decay must be at least $2m_e$ lower than in the case of a $2\nu\beta^-\beta^-$ decay. This implies that $2\nu\beta^+\beta^+$ -decaying isotopes are more rare than $2\nu\beta^-\beta^-$ -decaying isotopes. Moreover, for the same energy difference between the ground states of the intermediate and final nuclei, the energy difference between the ground states of the initial and final nucleus in a $2\nu\beta^+\beta^+$ decay is at least $2m_e$ lower than in the case of a $2\nu\beta^-\beta^-$ decay, leading to a correspondingly smaller Q-value. For these reasons, $2\nu\beta^+\beta^+$ decay has been less studied than $2\nu\beta^-\beta^-$ decay and in the following we will consider only $2\nu\beta^-\beta^-$ decays (from now on we will simply refer to them with $2\nu\beta\beta$). Let us only mention that $\mathcal{N}(A, Z) \rightarrow \mathcal{N}(A, Z - 2)$ transitions can occur not only through $2\nu\beta^+\beta^+$ processes, but also through the processes

$$\begin{aligned} e^- + \mathcal{N}(A, Z) &\rightarrow \mathcal{N}(A, Z - 2) + e^+ + 2\nu_e & [\text{EC}\beta^+] \\ 2e^- + \mathcal{N}(A, Z) &\rightarrow \mathcal{N}(A, Z - 2) + 2\nu_e & [2\text{EC}2\nu] \end{aligned} .$$

The rate of $2\nu\beta\beta$ can be calculated by invoking the recipe of the Fermi golden rule for simple β decay. To a good approximation, the kinematic part (the phase space of the leptons emitted in the decay) and the nuclear part (the matrix element responsible for the transition probability between two nuclear states) can be factorized as

$$\Gamma^{2\nu} = G^{2\nu}(Q_{\beta\beta}, Z)|\mathcal{M}^{2\nu}|^2 , \quad (2)$$

where $G^{2\nu}$ is obtained by integration over the phase space of four leptons emitted in the decay and can be calculated exactly. The nuclear matrix element $\mathcal{M}^{2\nu}$ deals with the nuclear structure of the transition and is much more difficult to evaluate.

Denoting the 4-momentum of the two electrons and the two anti-neutrinos by $p_i^\alpha = (E_i, \mathbf{p}_i)$ and $q_i^\alpha = (\omega_i, \mathbf{q}_i)$, respectively ($i = 1, 2$), the relevant matrix element is given by

$$i\mathcal{M} = iG_F^2 V_{ud}^2 [\bar{u}(p_1)\gamma^\mu(1 - \gamma_5)v(q_1)][\bar{u}(p_2)\gamma^\nu(1 - \gamma_5)v(q_2)]J_{\mu\nu} - (p_1 \leftrightarrow p_2) . \quad (3)$$

The hadronic tensor $J_{\mu\nu}$ corresponds to the product of two nuclear currents written in the impulse approximation [3]. Including the implementation of the long-wave and closure approximation for the hadronic tensor [3], we obtain

$$\sum_{\text{spin}} |\mathcal{M}|^2 = 64G_F^4 |V_{ud}|^4 g_A^4 (p_1 \cdot p_2) (q_1 \cdot q_2) |\mathcal{M}^{2\nu}|^2 , \quad (4)$$

where the nuclear matrix element involves vector and axial couplings for Fermi and Gamow-Teller transitions in the form

$$g_A^2 \mathcal{M}^{2\nu} = g_V^2 \mathcal{M}_F^{2\nu} - g_A^2 \mathcal{M}_{GT}^{2\nu} . \quad (5)$$

General methods for phase-space factor calculations in double-beta decay have been developed [3, 5, 6]. The decay rate is given by integrating over all possible energies and angles of the leptons emitted in the decay. For the two-neutrino mode, these leptons are the two electrons and the two anti-neutrinos:

$$\begin{aligned} d\Gamma = & \frac{1}{4} \int \frac{d^3 p_1}{(2\pi)^3 2E_1} \frac{d^3 p_2}{(2\pi)^3 2E_2} \frac{d^3 q_1}{(2\pi)^3 2\omega_1} \frac{d^3 q_2}{(2\pi)^3 2\omega_2} \\ & \times F(Z, E_1) F(Z, E_2) \sum |\mathcal{M}|^2 \\ & \times 2\pi \delta(E_1 + E_2 + \omega_1 + \omega_2 - E_F + E_I) , \end{aligned} \quad (6)$$

where $F(Z, E)$ is the Fermi function that describes the Coulomb effect on the outgoing electrons and E_I, E_F are the energies of the parent and the daughter nucleus, respectively.

In the Primakoff-Rosen approximation [7] for the non-relativistic Coulomb correction, the sum spectrum of the electrons energies can be analytically calculated. After a suitable change of integration variables, defining the sum of kinetic energies $K = T_1 + T_2$ for the two electrons and integrating over the remaining variables, we obtain

$$\frac{d\Gamma}{dK} = \Lambda \cdot (K^5 + 10K^4 + 40K^3 + 60K^2 + 30K)(Q_{\beta\beta} - K)^5 , \quad (7)$$

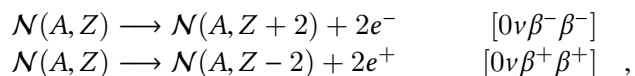
where K is written in units of the electron mass. The overall constant factor is given by

$$\Lambda = \frac{G_F^4 g_A^4 |V_{ud}|^4 F_{\text{PR}}^2(Z) m_e^{11}}{7200\pi^7} |\mathcal{M}^{2\nu}|^2 , \quad (8)$$

with $F_{\text{PR}}(Z) = 2\pi\alpha/Z(e^{-2\pi\alpha Z})$. The distribution for ${}^{76}\text{Ge}$ is plotted in Fig. 3.

The neutrinoless double-beta decay

The neutrinoless double-beta decay processes ($0\nu\beta\beta$) of the types



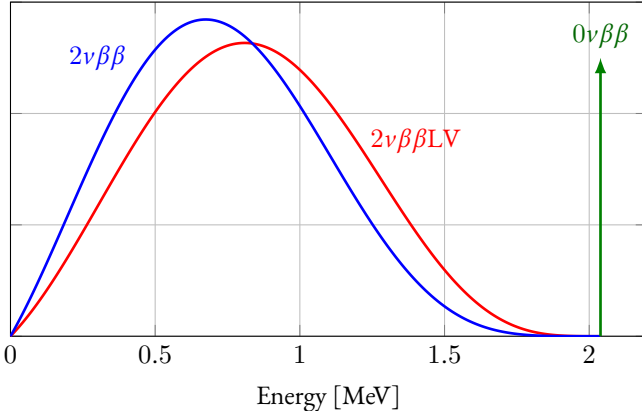


Figure 3: Energy spectra for different double-beta decay modes of ^{76}Ge : the two-neutrino mode (blue), the Lorentz violating mode (red), the neutrinoless mode (green).

which have been proposed by W. H. Furry in 1939 [8], are forbidden in the minimal Standard Model, where the neutrinos are massless, because the conservation of the total lepton number is violated by two units. Considering that today we know, from oscillations experiments, that neutrinos are instead massive particles, there are two ways to characterize them: they could be Dirac (as all the other fundamental particles) or Majorana particles. Being a Majorana particle, as first proposed by Ettore Majorana [9], basically means do not distinguish between particle and anti-particle. $0\nu\beta\beta$ decays, in the standard interpretation, are possible if neutrinos are massive Majorana particles, with the Feynman diagram in Fig. 1, right. In this case, no neutrinos are emitted during the process and the experimental signature is a Dirac-delta function at $Q_{\beta\beta}$ in the summed energy spectrum (Fig. 3). A nucleus which can decay through a $2\nu\beta\beta$ process can also decay through a $0\nu\beta\beta$ process, albeit with a different lifetime ($\gtrsim 10^{25}$ yr). Also the other double-beta decay modes mentioned above have their neutrinoless analog. However, as reviewed in [10], it should be pointed out that there are many other well-motivated Particle Physics scenarios and frameworks that allow for $0\nu\beta\beta$, treated as negligible contributions in the standard interpretation.

Considerable experimental efforts are being dedicated to the detection of $0\nu\beta\beta$, as such experiments represent the only practical way of establishing the nature of neutrino mass and therefore of shedding light on the mechanism of the tiny (but non-zero) neutrino mass generation established by neutrino oscillation experiments.

The Lorentz violating two-neutrino double-beta decay

Since the Standard Model of Particle Physics is known to provide a successful description of most Physics at low energies, compared to the Planck scale $m_p \sim 10^{19}$ GeV, any signal of new Physics must appear at low energies in the form of an effective quantum field theory containing the Standard Model. The general effective quantum field theory

constructed from the latter and allowing for arbitrary coordinate-independent Lorentz violation is called the Standard Model Extension [11, 12]. As an effective field theory it provides a link to the Planck scale through operators of non-renormalizable dimension. The Lagrangian of the Standard Model Extension consists of the usual Standard Model Lagrangian supplemented by all possible terms that can be constructed with the existing fields and that introduce violations of Lorentz symmetry. The additional terms have the form of Lorentz-violating operators coupled to vector coefficients, and they could arise in a variety of ways.

All quantum field operators for Lorentz violation involved in the propagation of neutrinos have been classified and enumerated [13]. Most of these can be studied using neutrino oscillations, which compare the way different neutrinos propagate and provide interferometric sensitivity to energy differences between them. Some effects cannot be detected by neutrino oscillations because they are produced by ‘oscillation-free’ operators that change all neutrino energies equally. Most of these can instead be studied by comparing neutrino propagation to other species, such as time-of-flight experiments matching the group velocity of neutrinos with the photons’ one. However, four oscillation-free operators leave unaffected the neutrino group velocity and so cannot be detected in this way. Instead, they must be accessed through physical processes that involve neutrino phase-space properties, such as particle decays. These operators are rare examples of *countershaded* Lorentz violations [14]: Relativity-violating effects that could be enormous compared to ones suppressed by the ratio m_W/m_P and that nonetheless could have escaped detection to date. These could provide an interesting path for building models with viable Lorentz violation obviating the typical requirement of a heavy suppression factor.

The four countershaded neutrino operators are of renormalizable mass dimension $d = 3$, are odd under CPT, and are controlled by coefficients conventionally denoted with $(a_{\text{of}}^{(3)})_{jm}$, where j, m are angular-momentum quantum numbers with $j = 0, 1$. Conservation of energy and momentum is assured by taking these four coefficients to be constant as usual for couplings beyond the Standard Model, so all Physics other than Lorentz and CPT violation is conventional. Dimensional arguments suggest these coefficients are likely to dominate at accessible energies and can be measured sensitively in low-energy processes.

The anti-neutrino phase space element d^3q is modified by the presence of these new operators:

$$\omega^2 d\omega d\Omega \mapsto f(\omega) d\omega d\Omega , \quad (9)$$

where the anti-neutrino function

$$f(\omega) \simeq \omega^2 - \frac{1}{2}m_v^2 - 2\omega\delta\omega \quad (10)$$

encodes the Lorentz-violating modifications

$$\delta\omega = - \sum_{jm} e^{im\omega_\oplus T_\oplus} N_{jm} (a_{\text{of}}^{(3)})_{jm} \quad (11)$$

arising from the modified anti-neutrino dispersion relation [13] $\omega = |\mathbf{q}| + m_\nu^2/|\mathbf{q}| + \delta\omega$. The sidereal time T_\oplus controls the harmonic variation of the anti-neutrino function in the laboratory produced by the Earth sidereal rotation at frequency $\omega_\oplus \simeq 2\pi/(23 \text{ h } 56 \text{ min})$. The factors N_{jm} contain information about the direction of propagation of the anti-neutrinos, expressed relative to the canonical sun-centered frame of reference [15, 16].

Following the same procedure as in the conventional two-neutrino double-beta decay, we integrate over all orientation, which implies that only isotropic effects are observable and hence that the residual spectrum depends only on $\dot{\bar{a}}_{\text{of}}^{(3)} \equiv (\bar{a}_{\text{of}}^{(3)})_{00}/\sqrt{4\pi}$. After a suitable change of integration variables and defining the sum of kinetic energies $K = T_1 + T_2$ for the two electrons, we obtain the electron sum spectrum

$$\frac{d\Gamma}{dK} = \Lambda \cdot (K^5 + 10K^4 + 40K^3 + 60K^2 + 30K) \times [(Q_{\beta\beta} - K)^5 + 10\dot{\bar{a}}_{\text{of}}^{(3)}(Q_{\beta\beta} - K)^4]. \quad (12)$$

The total decay rate can be therefore expressed as an addition of two separate rates through a perturbation:

$$\Gamma = \Gamma_0 + \delta\Gamma, \quad (13)$$

where the first term is (7) and the second one contains all the new Lorentz-violating information. The two differential decay rates are depicted in Fig. 3.

Current limits on $\dot{\bar{a}}_{\text{of}}^{(3)}$

Conservative constraints on the $(\dot{\bar{a}}_{\text{of}}^{(3)})_{00}$ coefficient have been placed using published results from the Troitsk and Mainz experiments studying the endpoint of the tritium beta decay energy spectrum [17]. An outside analysis of data from the two experiments gives $|(\dot{\bar{a}}_{\text{of}}^{(3)})_{00}| < 2 \cdot 10^{-8} \text{ GeV}$ for both of them. Constraints on the values of $\dot{\bar{a}}_{\text{of}}^{(3)}$ have also been extracted from studies of threshold effects in pion and kaon decays [13], yielding $\dot{\bar{a}}_{\text{of}}^{(3)} < 1.9 \cdot 10^{-7} \text{ GeV}$ as the best upper limit.

A constraint from double-beta decay studies has been posed by the EXO-200 collaboration in Ref. [18]. A profile Likelihood scan over the number of Lorentz-violating double beta decay integral counts added to the standard $2\nu\beta\beta$ spectrum is used to obtain a limit at the 90% C.L., which is $\dot{\bar{a}}_{\text{of}}^{(3)} < 7.6 \cdot 10^{-6} \text{ GeV}$. This is the first search for this parameter that fully accounts for experimental backgrounds and detector-related systematic uncertainties.

2 The GERDA experiment

The GERDA experiment [19] (GERmanium Detector Array) is dedicated to the search of the neutrinoless double-beta decay ($0\nu\beta\beta$) of ^{76}Ge . As mentioned in §1, the half-lives for $0\nu\beta\beta$ decay, assuming the process exists, are expected to be substantially longer than the corresponding $2\nu\beta\beta$ ones, consequently, $0\nu\beta\beta$ decay experiments must be sensitive to just a few events per year for a source with a mass of tens to hundreds of kilograms. Backgrounds must typically be reduced to the level of one event per year in an energy interval of the order of the energy resolution around $Q_{\beta\beta}$.

Experiments looking for $0\nu\beta\beta$ decay of ^{76}Ge operate germanium diodes normally made from enriched material, i.e. the number of ^{76}Ge nuclei, the isotopic fraction f_{76} , is enlarged from 7.8% to 86% or higher. In these type of experiments, the source is equal to the detector which yields high detection efficiency. Additional advantages of this technique are the superior energy resolution of 0.2% at $Q_{\beta\beta} = 2039$ keV compared to other searches with different isotopes and the high radiopurity of the crystal growing procedure. Disadvantages are the relatively low $Q_{\beta\beta}$ value since backgrounds typically fall with energy and the relative difficulty to scale to larger mass compared to e.g. experiments using liquids and gases.

GERDA has been built in the INFN Laboratori Nazionali del Gran Sasso (LNGS) at a depth of 3500 m w.e. (water equivalent) and submerses bare high-purity germanium detectors enriched in ^{76}Ge into liquid argon (LAr). LAr serves simultaneously as a shield against external radioactivity and as a cooling medium. Phase I of the experiment was intended to give a statistically unambiguous statement concerning the observation of the

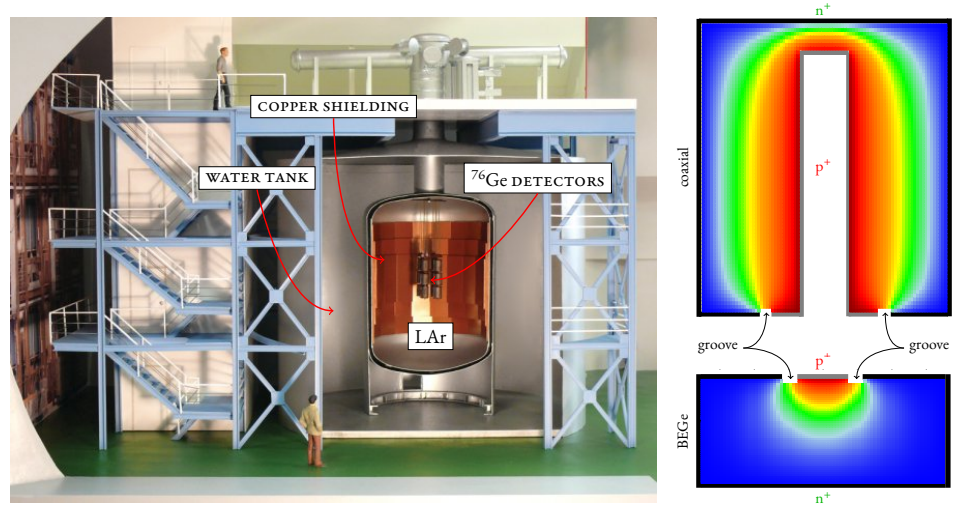


Figure 4: On the right: artists view (Ge array not to scale) of the GERDA experiment. On the left: scheme of the coaxial and BEGe detectors deployed in GERDA. On the top the p-type HPGe, on the bottom the BEGe type. The weighting potential is also showed with a color gradient.



Figure 5: Inside the water tank after the installation of the muon veto system — August 2009, photo courtesy of Markus Knapp *et al.*

neutrinoless double-beta decay claimed by a subgroup of the HDM collaboration [20]. It ended in May 2013 with a total exposure of $21.6 \text{ kg}\cdot\text{yr}$, and the analysis reported no excess of events above the background at $Q_{\beta\beta}$ [21]. More recently the statement was confirmed also by the addition of the first data from Phase II [22], that allowed to reach a $34.4 \text{ kg}\cdot\text{yr}$ exposure and improve the limit on the half-life up to

$$T_{1/2}^{0\nu} > 5.3 \cdot 10^{25} \text{ yr} \quad (90\% \text{ C.L.}) . \quad (14)$$

Phase II of GERDA is expected to further improve the sensitivity up to 10^{26} yr .

The main feature of the GERDA design is to operate bare germanium detectors made out of material enriched in ${}^{76}\text{Ge}$ (${}^{\text{enr}}\text{Ge}$) in LAr. It allows for a significant reduction in the cladding material around the diodes and the accompanying radiation sources as compared to traditional germanium experiments. Furthermore, the background produced by interactions of cosmic rays is lower than for the traditional concepts due to the lower atomic number of the shielding material. Other background sources include neutrons and gammas from the decays in the rock of the underground laboratory, radioactivity in support materials, radioactive elements in the cryogenic liquid as well as internal backgrounds in the germanium diodes. Natural Ge (${}^{\text{nat}}\text{Ge}$) contains about 7.8% ${}^{76}\text{Ge}$, and could in principle be used directly for a $0\nu\beta\beta$ decay experiment. However enriched detectors allow for a better signal-to-background ratio and also yield reduced costs for a fixed mass of ${}^{76}\text{Ge}$ in the experiment.

DESIGN
AND
GENERAL
LAYOUT

Fig. 4 (left) shows a model of the realized design: the core of the experiment is an array of germanium diodes suspended in strings into a cryostat filled with LAr. The LAr serves both as cooling medium and shield. The cryostat is a steel vessel with a copper

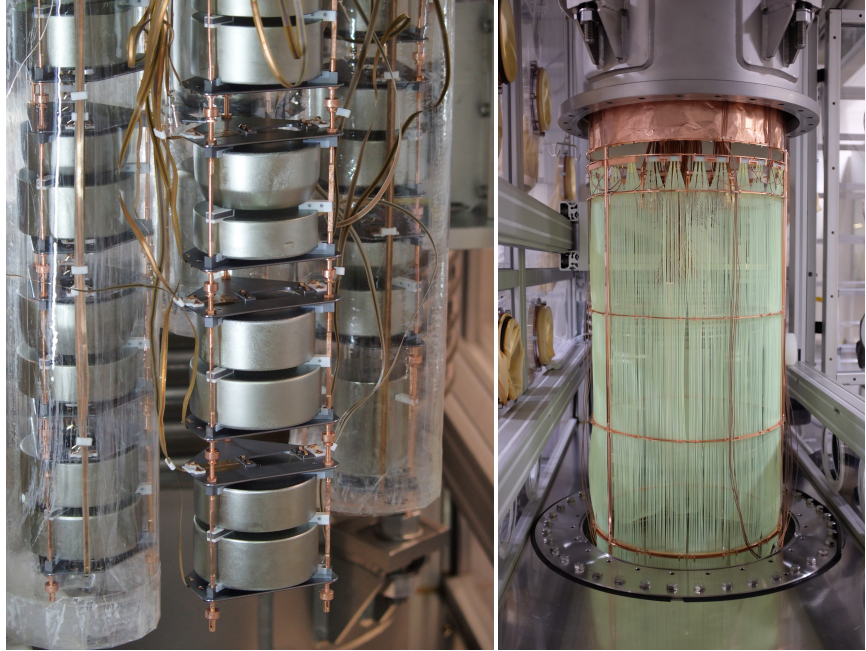


Figure 6: On the left: some detector strings — final integration in July 2015, photo courtesy of Bernhard Schwingenheuer. On the right: the fiber-shroud being deployed in LAr — November 2015, photo courtesy of Mark Heisel.

lining used primarily to reduce the gamma radiation from the steel vessel. The cryostat is placed in a large water tank, that fulfills the functions of shielding the inner volumes from radiation sources within the hall, such as neutrons, as well as providing a sensitive medium for a muon veto system (Fig. 5), comprehensive of a set of scintillating panels on the top of the apparatus. The detectors are lowered into the LAr volume using a lock system located in a clean room on top of the water tank. A further muon veto system is placed on top of the clean room in order to shield the neck region of the cryostat. A detailed description of the experimental setup for Phase I is provided in [19].

Phase II came with some upgrades to improve the background rejection performance. The volume directly surrounding the detector array was instrumented with photo-multipliers to detect the scintillation light emitted if energy is deposited inside LAr. This allows to identify background events resulting from Compton scattered photons with partial energy deposit in the detectors and partial energy deposit inside the LAr. Additionally, a curtain made from light guide fibers with Tetraphenyl butadiene (TPB) deposited on their surface was built to surround the detector array (Fig. 6, right). Photons reaching the light guides are wavelength shifted and guided to the end of the fibers, where they can be detected by silicon photo-multipliers (SiPMs) optically coupled to the fibers. The new components improve the efficiency in the identification of background events, as proved in [22]. In Phase I the individual detector strings were surrounded by a copper shroud, minimizing the LAr volume from which ^{42}K ions, that strongly contribute to the

background, can be collected on the detector surfaces. Additionally the shrouds were set to ground potential to minimize drift towards the detectors. In order to take maximum advantage of the light instrumentation of the LAr, in Phase II the copper shroud has been exchanged by a transparent TPB-coated shroud (called mini-shroud) that allows to minimize the volume from which ^{42}K ions are collected, while allowing to detect scintillation light also from the volume inside the mini-shroud. Last but not least, 30 new BEGe detectors were deployed into the LAr.

For Phase I detectors ANG1, ANG2, ANG3, ANG4, ANG5 from the HDM [23] and RG1, RG2, RG3 from the IGEX [24] collaborations were refurbished and redeployed, in addition to three detectors made of $^{\text{nat}}\text{Ge}$ from the GENIUS-TF experiment [25, 26], GTF112, GTF45 and GTF32. A background level of an order of magnitude lower than in those former experiments was achieved. For Phase II new material was purchased in order to produce new diodes, and another factor of ten in background reduction was accomplished [22].

In p-type detectors the dimensionless ‘weighting potential’ Φ peaks close to the p^+ electrode. Ionization creates electrons and holes which drift due to the applied potential and the field created by the space charge of the depleted diode. The time dependent induced current $I(t)$ on the p^+ electrode is given by the Ramo-Shockley theorem [27] as:

$$I(t) = q \cdot \mathbf{v}(\mathbf{r}(t)) \cdot \nabla \Phi(\mathbf{r}(t)), \quad (15)$$

where q stands for the drifting charge and $\mathbf{v}(\mathbf{r}(t))$ for the drift velocity at position $\mathbf{r}(t)$.

Phase I detectors are based on standard p-type HPGe detector technology from Canberra Semiconductor NV, Olen¹. Standard closed-end coaxial detectors have a ‘wrap around’ n^+ conductive lithium layer ($\sim 1 \text{ mm}$) that is separated from the boron implanted p^+ contact by a groove; the groove region is usually passivated. The detector geometry for one of the enriched detectors is shown schematically in Fig. 4 (right). In normal DC coupled readout, the p^+ contact ($\sim 1 \mu\text{m}$) is connected to a charge sensitive amplifier and the n^+ surface is biased with up to +4600 V.

GERDA has chosen a modified thick window Broad Energy Germanium (BEGe) detector manufactured by Canberra as the detector type for Phase II. A batch of 37.5 kg of $^{\text{enr}}\text{Ge}$ was procured by the Electrochemical Plant (ECP) in Železnogorsk, Russia² in 2005 and delivered in the form of $^{\text{enr}}\text{GeO}_2$ to the company PPM Pure Metals GmbH³ in Langelsheim, Germany, to be reduced and further purified. For further zone refinement and crystal growth the 35.5 kg of purified enriched germanium was sent to Canberra Industries Inc.⁴, Oak Ridge (TN), USA. The conversion of the 30 germanium crystal slices into operational BEGe detectors was performed at Canberra Semiconductors NV, Olen, Belgium. Out of 53.4 kg of GeO_2 , containing 37.5 kg of elemental enriched germanium,

¹Canberra Semiconductors, NV, Lammerdries 25, B-2250, Olen, Belgium; <http://www.canberra.com/>

²Currently known as Joint Stock Company ‘Production Association Electrochemical Plant’ (JSC ‘PA Electrochemical Plant’), uranium enrichment enterprise of the State Atomic Energy Corporation ‘Rosatom’.

³PPM Pure Metals GmbH, Am Bahnhof 1, 38685 Langelsheim, Germany; <http://www.pppuremetals.de/>.

⁴Canberra Industries Inc., 107 Union Valley Rd, Oak Ridge, TN, USA; <http://www.canberra.com/>

30 detectors with a total mass of 20.0 kg were fabricated. One crystal slice (GD02D) turned out to have a non satisfactory impurity distribution. This detector does not reach full depletion and the corresponding voltage plateau; therefore it has a deteriorated charge collection efficiency in some parts of the crystal. Nonetheless, this detector has been deployed in GERDA Phase II; its full or partial inclusion into the analysis can be decided later. Cosmogenically produced isotopes ^{68}Ge and ^{60}Co can lead to an internal contamination that represents a background in the region of interest. The detectors are always stored at an underground facility to avoid exposure to cosmic rays⁵. All the new BEGe detectors were deployed in LAr together with the Phase I detectors during the final integration in July 2015, and RG3 was removed from apparatus since it was operated below its full depletion voltage.

Compared to the semi-coaxial detectors used in GERDA Phase I, the BEGe detector design shows smaller dimensions and thus smaller mass. Due to a different layout of the electrodes (see Fig. 4) the electric field profile in BEGe detectors differs strongly from the one in semi-coaxial detectors. They are made of p-type germanium, comprising a ‘wrap around’ n^+ electrode known as ‘lithium dead layer’, a p^+ electrode acting as electron blocking contact, and an intercontact insulating surface. For the third item a small annular concentric groove between the p^+ and n^+ electrodes is produced and covered by an insulating silicon monoxide layer which is known as ‘passivation layer’. This layer helps to keep steady-state currents (so-called ‘leakage currents’) stable over time. Holes drift to the p^+ electrode along the region around the central axis, irrespective of the starting point (‘funnel’ effect); $I(t)$ peaks at the end of the drift where $\nabla\Phi$ is largest. Hence, the maximum A of $I(t)$ is directly proportional to the deposited energy E . Electrons drift through volumes with low $\nabla\Phi$ and hardly contribute to A . That means that A/E is constant for all single-site events except for ionizations in a small volume close to the p^+ electrode [28–30]. In contrast, for multi-site events the drift times of holes from several simultaneous energy depositions are in general different and hence A/E of the summed signal is reduced. For ionizations in the n^+ transition layer (like from surface β -events) the diffusion time is comparable to the drift time and hence A/E is also reduced. For p^+ surface events electrons drift through the volume with largest $\nabla\Phi$, and hence A/E is larger than for single-site events due to the increased displacement current. The latter is also the case for events close to the groove. Since it is known that signal events from $0\nu\beta\beta$ decays deposit energy within a small volume (if the electrons lose little energy by bremsstrahlung), and, on the contrary, in background events energy is often deposited at several locations well separated by a few cm in the detector, the A/E parameter can be used to discriminate between the two situations. A detailed description of the production, characterization and operation of the BEGe detectors in GERDA is given in [31], while the pulse shape discriminating techniques adopted for Phase I analysis are presented in [32]. Some relevant properties of the detectors deployed in GERDA are given in Tab. 1 and 2.

The mounting scheme of the detectors has competing requirements. It must have a low mass to minimize sources of radiation near to the detectors. However, the construc-

⁵High Activity Disposal Experimental Site (HADES) of the Belgian Nuclear Research Center SCK·CEN, Boeretang 200, BE-2400 Mol, Belgium.

tion must be sufficiently sturdy to provide safe suspension. It must support the cables for detector bias and readout. Furthermore, the diodes must remain electrically isolated from all other materials. The chosen support design can be appreciated in Fig. 6 (left). In order to reach the background goals of GERDA, the amount of material is minimized. Only selected high radiopurity materials were used: copper, PTFE and silicon.

An important source of background is induced by cosmic radiation. Muon induced background events are efficiently vetoed by identification of Čerenkov light emitted by muons when they pass the water tank or the LAr. The number of long lived cosmogenically produced isotopes, especially ^{68}Ge and ^{60}Co are minimized by minimization of the time above ground during processing of the detectors and the structural materials. Further background contributions stem from radioactivity included in the detector and structural materials or the surrounding environment, i.e. the rocks of the laboratory.

Background from ^{42}Ar present in LAr was found during GERDA commissioning to be more significant than anticipated. The β -decay of its progeny ^{42}K can contribute to the background in the RoI if the decay happens near detector surfaces. For coaxial detectors this background was significantly reduced by implementation of the mini-shroud around the germanium strings. However, for the BEGe detectors this remains an important background due to their thinner surface n^+ dead layer. The β^- decay of the ^{39}Ar is also a strong component of the energy spectrum, however his Q-value is far below the RoI, at $Q_\beta = 565 \text{ keV}$.

Another potential source of background stems from the calibration sources that have a typical initial activity of about 10–20 kBq. When in parking position they are well shielded and contribute insignificantly.

A significant fraction of the background is induced by contaminations of bulk materials and surfaces with nuclei from the ^{238}U and ^{232}Th decay chains. The ^{238}U decay chain can be subdivided into three sub decay chains: ^{238}U to ^{226}Ra , ^{226}Ra to ^{210}Pb and ^{210}Pb to ^{206}Pb , due to isotopes with half lives significantly longer than the live time of the experiment. Only the two latter sub decay chains are relevant in the following. The noble gas ^{222}Rn ($T_{1/2} = 3.8$ days) plays a special role, as it can further break the ^{226}Ra to ^{210}Pb chain due to its volatility. Whenever activities of ^{214}Bi are quoted it is assumed that the chain is in secular equilibrium between ^{226}Ra and ^{210}Pb inside metallic materials, while for non metallic materials the equilibrium can be broken at ^{222}Rn .

Table 1: Some relevant properties, taken from [33, 34], of the detectors deployed in GERDA for Phase II. The mass, the enrichment fraction f_{76} , the active volume fraction f_{av} and the FWHM at the ^{228}Tl peak at 2614 keV are reported. A field is left empty when no information is available.

Detector	Mass [g]	f_{76}	f_{av}	FWHM [keV]
GTF32	2321	0.087(1)	0.97(5)	3.49
GTF45	2312	0.087(1)	–	2.86
GTF112	2965	0.087(1)	–	4.36
RG1	2110	0.855(15)	0.904(59)	2.92
RG2	2166	0.855(15)	0.831(53)	2.63
ANG1	958	0.859(29)	0.830(52)	3.64
ANG2	2833	0.866(25)	0.871(51)	5.42
ANG3	2391	0.883(26)	0.866(57)	2.92
ANG4	2372	0.863(13)	0.901(57)	3.51
ANG5	2746	0.856(13)	0.831(48)	2.88
GD00A	496	0.877(13)	$0.886^{+0.018}_{-0.018}$	2.93
GD00B	697	0.877(13)	$0.880^{+0.018}_{-0.017}$	3.07
GD00C	815	0.877(13)	$0.892^{+0.018}_{-0.016}$	3.12
GD00D	813	0.877(13)	$0.889^{+0.017}_{-0.016}$	2.83
GD02A	545	0.877(13)	$0.896^{+0.015}_{-0.014}$	2.67
GD02B	625	0.877(13)	$0.885^{+0.017}_{-0.016}$	2.81
GD02C	788	0.877(13)	$0.888^{+0.017}_{-0.016}$	2.82
GD02D	662	0.877(13)	$0.834^{+0.016}_{-0.016}$	2.93
GD32A	458	0.877(13)	$0.882^{+0.022}_{-0.021}$	2.61
GD32B	716	0.877(13)	$0.883^{+0.015}_{-0.014}$	2.83

Table 2: Some relevant properties, taken from [33, 34], of the detectors deployed in GERDA for Phase II. The mass, the enrichment fraction f_{76} , the active volume fraction f_{av} and the FWHM at the ^{228}Tl peak at 2614 keV are reported.

Detector	Mass [g]	f_{76}	f_{av}	FWHM
GD32C	743	0.877(13)	$0.895^{+0.015}_{-0.014}$	2.83
GD32D	720	0.877(13)	$0.913^{+0.016}_{-0.014}$	3.35
GD35A	768	0.877(13)	$0.902^{+0.017}_{-0.017}$	2.83
GD35B	810	0.877(13)	$0.914^{+0.015}_{-0.014}$	2.91
GD35C	634	0.877(13)	$0.902^{+0.016}_{-0.015}$	2.60
GD61A	731	0.877(13)	$0.892^{+0.017}_{-0.016}$	2.95
GD61B	751	0.877(13)	$0.887^{+0.017}_{-0.016}$	3.54
GD61C	634	0.877(13)	$0.887^{+0.017}_{-0.016}$	2.96
GD76B	384	0.877(13)	$0.848^{+0.020}_{-0.018}$	2.96
GD76C	824	0.877(13)	$0.878^{+0.016}_{-0.015}$	2.84
GD79B	736	0.877(13)	$0.881^{+0.019}_{-0.018}$	3.36
GD79C	812	0.877(13)	$0.878^{+0.015}_{-0.014}$	3.97
GD89A	524	0.877(13)	$0.882^{+0.020}_{-0.018}$	3.42
GD89B	620	0.877(13)	$0.859^{+0.020}_{-0.019}$	2.86
GD89C	595	0.877(13)	$0.874^{+0.022}_{-0.019}$	2.90
GD89D	526	0.877(13)	$0.863^{+0.020}_{-0.018}$	2.83
GD91A	627	0.877(13)	$0.889^{+0.017}_{-0.017}$	2.71
GD91B	650	0.877(13)	$0.889^{+0.017}_{-0.016}$	2.93
GD91C	627	0.877(13)	$0.887^{+0.018}_{-0.017}$	2.53
GD91D	693	0.877(13)	$0.888^{+0.018}_{-0.017}$	3.14

3 Data and simulations

The raw data is processed to produce a set of events which is suitable for comparison with theoretical expectations. In this section we treat how the data is structured and purified from unphysical or unwanted events, then the shapes of the resulting energy spectra, used to fit the theoretical distributions, are presented. The results from the material screening, that will be used to constrain the analysis, are given. Finally, the Monte Carlo simulations, carried out for this analysis, that represent the $2\nu\beta\beta$ and the background contributions in the data are detailed.

The GERDA data set

THE
GERDA
DATA
STRUCTURE

In general the binary raw data format is custom defined by the different data acquisition systems. In order to optimize the analysis streaming and to provide a unique input interface for the analysis, all raw data is converted to a common standardized format. MGDO [35] (MAJORANA GERDA Data Objects) is a software library jointly developed by GERDA and MAJORANA [36]. The core function of this software is to provide a collection of C++ objects to encapsulate HPGe detector array event data and related analytical quantities. It also includes implementations of a number of general-purpose signal processing algorithms to support advanced detector signal analysis. The custom data objects available in the MGDO package are used as a reference format to store events, waveforms, and other DAQ data (time stamps, flags). The MGDO data objects are stored as ROOT [37] files. The set of ROOT files produced by the conversion of raw data is named TIER1, and is officially distributed for the analysis.

Since the information contained in the TIER1 set and in the raw data is expected to be equal, the conversion procedure is the optimal place where blinding can be applied. Events with an energy within ± 25 keV around $Q_{\beta\beta}$ are not exported to TIER1 but they remain saved in the backup of the raw data.

The software framework GELATIO [38] contains nearly independent and customizable modules that are applied to the input TIER1 waveforms. The results (pulse amplitude, rise time, average baseline, energy, etc.) are stored as a new ROOT file (TIER2). A description of the analysis modules is presented in Ref. [39]. Higher level TIER*i* files that contain additional parameters evaluated from more advanced analysis (e.g. calibrated energy spectra) can be created. In principle only the TIER1 is official and every analysis should produce his own TIER2 files depending on the actual needs. However there exists a ‘reference’ TIER2 produced with a standard set of GELATIO modules with a reasonable choice of parameters (e.g. the width of the gaussian filter responsible for the reconstruction of the energy of an event) that can be used in most situations. The same reference data sets are provided for every TIER*i* level.

Once the relevant quantities have been extracted from raw waveforms they have to be calibrated (e.g. energy) and quality cuts (e.g. to reject unphysical events) have to be applied. The results are again stored as a ROOT file (TIER3). The extraction of parameters related to the entire event (e.g. the number of channels with a physical signal) is also performed

at this level. Finally, high-level quality cuts are applied in TIER4, such as pulse shape discrimination, muon-veto and LAr-veto.

The data selection procedure undergoes various steps in order to purify the data set from unphysical or unwanted events. In the following all the classes of events excluded from the analysis are presented.

- ◊ There is a set of classes of events that originates from failures in the acquisition process or in the reconstruction process (e.g. a failure of a GELATIO module) and thus must be tagged and removed.
- ◊ A cut must also be applied on events not related to an energy deposition, and thus consisting of a flat signal (an energy deposition in one detector triggers the sampling of the pulses registered in all detectors, so it is very common to find pure-baseline signals in data), waveforms which amplitude exceeds the FADC's energy threshold (overshoot events), and pile-up events.
- ◊ The main purpose for acquiring pulses from all the detectors when an energy deposition occurs anywhere is to provide the ability to discriminate multi-detector events. Such events cannot be associated to the detection of double-beta decay electrons, which are usually absorbed within the detector's volume, and thus they can be discarded as background events.
- ◊ Events that leave a trace also in the water tank and/or in the upper scintillating panels and thus flagged by the muon-veto system are also discarded.

The summed energy spectra from BEGe, enriched coaxial and natural coaxial detectors after the application of the quality cuts are presented in Fig. 9. The considered data set was taken between December 2015 and March 2017. Some prominent features can be identified. The low energy part up to 565 keV is dominated by β^- decay of cosmogenic ^{39}Ar in all spectra. Slight differences in the spectral shape between the coaxial and BEGe type detectors result from differences in detector geometry and of the n^+ dead layer thickness. Between 600 and 1500 keV the spectra of the enriched detectors exhibit an enhanced continuous spectrum due to $2\nu\beta\beta$ decay (see Fig. 3 for the theoretical curves). In all spectra, γ lines from the decays of ^{40}K and ^{42}K can be identified, and the spectra of the enriched coaxial detectors contain also lines from ^{208}Tl and ^{214}Bi . A small peak occurring at 969 keV can be attributed to the presence of ^{228}Ac . The peak-like structure around 5.3 MeV can be attributed to the α -decays near the detector p^+ surface.

The Background Index (BI), used to estimate the background activity in the ROI, is defined as the number of counts over detector's mass, live time and energy range inside a energy window defined as follows (see also Fig. 7). The window covers the energy range between 1930 keV and 2190 keV excluding the blinded window around $Q_{\beta\beta}$. Also the two lines from ^{208}Tl and ^{214}Bi occurring respectively at 2104 keV and 2119 keV are neglected in this computation; this is done removing the energy range within ± 5 keV around the peaks. The final width of the window is then 190 keV. In Tab. 3 the background indices for the three considered data sets are given.

QUALITY CUTS

THE ENERGY SPECTRA

BACKGROUND INDEX

SCREENING MEASUREMENTS

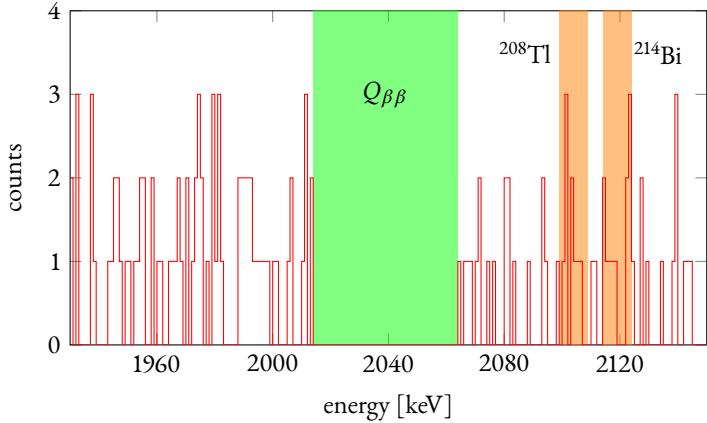


Figure 7: Energy window used to compute the background index, a 50 keV wide energy window around $Q_{\beta\beta}$ and two 10 keV wide energy windows around the ^{208}Tl and ^{214}Bi peaks are excluded. The displayed data corresponds to the whole GERDA data set.

There are some radioactive contaminations in the components of GERDA, though not evident in the energy spectra, which have been identified and systematically measured. The most relevant contributions, reported in Table 4, come from the silicon of the holder mounting, the cables, the nylon mini-shroud covering the detectors and the fiber-shroud. Measurements were performed with the ICP-MS mass spectroscopy or with a germanium detector (GeMPI) installed at LNGS.

Monte Carlo simulations

Background components that were identified in the energy spectra or that were known to be present in the vicinity of the detectors were simulated using the MAGE [40] code based on GEANT4 [41] and jointly developed by the GERDA and MAJORANA [36] collaborations. The detectors and the arrangement of the germanium detector array with seven detector strings were implemented into the MAGE code as well as the other GERDA components (see Fig. 8). During the simulation GEANT4 generates complete information about the trajectory and interactions of particles as they propagate through the detectors. All of this information is typically processed, parsed and saved to an output file for

Table 3: Background indices for the considered data sets.

DATA SET	BI 10^{-2} cts/(keV·kg·yr)
BEGe	1.16 ± 0.17
ENR COAX	1.72 ± 0.24
NAT COAX	2.76 ± 0.47

Table 4: Screening measurements for some of the considered GERDA components. The upper limits correspond to 90% C.L.

Location	Activities [mBq/kg]					
	^{40}K	^{228}Th	^{226}Ra	^{60}Co	$^{234\text{m}}\text{Pa}$	^{228}Ra
FIBER-SHROUD						
Fiber BCF-91A	0.46 ± 0.09	0.058 ± 0.012	–	–	$0.042 (^{238}\text{U})$	–
HOLDERS						
Si, V 3361/IKZ	4.3 ± 0.9	< 0.15	< 0.21	< 0.16	$< 9.7 (^{238}\text{U})$	< 0.39
CABLES						
Haefele 10 mils	109 ± 22	< 5.47	7.66 ± 2.2	–	< 365	< 8.4
Haefele 2 mils	220 ± 110	< 24.07	50 ± 11	–	< 2222	< 20.37
Tecnomec 3 mils	11 ± 3	< 0.46	< 0.38	–	< 44	< 0.56

further analysis after the simulation run is complete. Simulations of contaminations of the following hardware components were performed:

- ◊ on the p^+ and n^+ surfaces of the detectors;
- ◊ homogeneously distributed in the LAr, in a 17.7 m^3 cylinder centered in the detector array;
- ◊ in the detector assembly representing contaminations in the detector holders and their components;
- ◊ in the nylon mini-shroud surrounding the detectors;
- ◊ in the fiber-shroud;
- ◊ in the high-voltage cables and the signal cables.

The volumes representing the germanium array, the holder mounting and the cables are simulated as depicted in Fig. 8. The mini-shroud volume is implemented as a set of cylinders surrounding each detector string, while the fiber-shroud consists of the lateral surface of a cylinder.

The spectrum of the two electrons emitted in the $2\nu\beta\beta$ decay of ^{76}Ge is sampled according to the distribution of [42] that is implemented in the code DECAY0 [43]. The $2\nu\beta\beta$ decay distributions of [42] are in principle more precise than those based on the Primakoff-Rosen approximation [7], and they have been cross-checked against the high-statistics data of the NEMO experiment for several nuclei [44–48]. Electrons are propagated in the GERDA simulated setup by MAGe and the total energy released in the active mass of the enriched detectors is registered. The two spectra are shown in Fig. 10, top left.

^{40}K

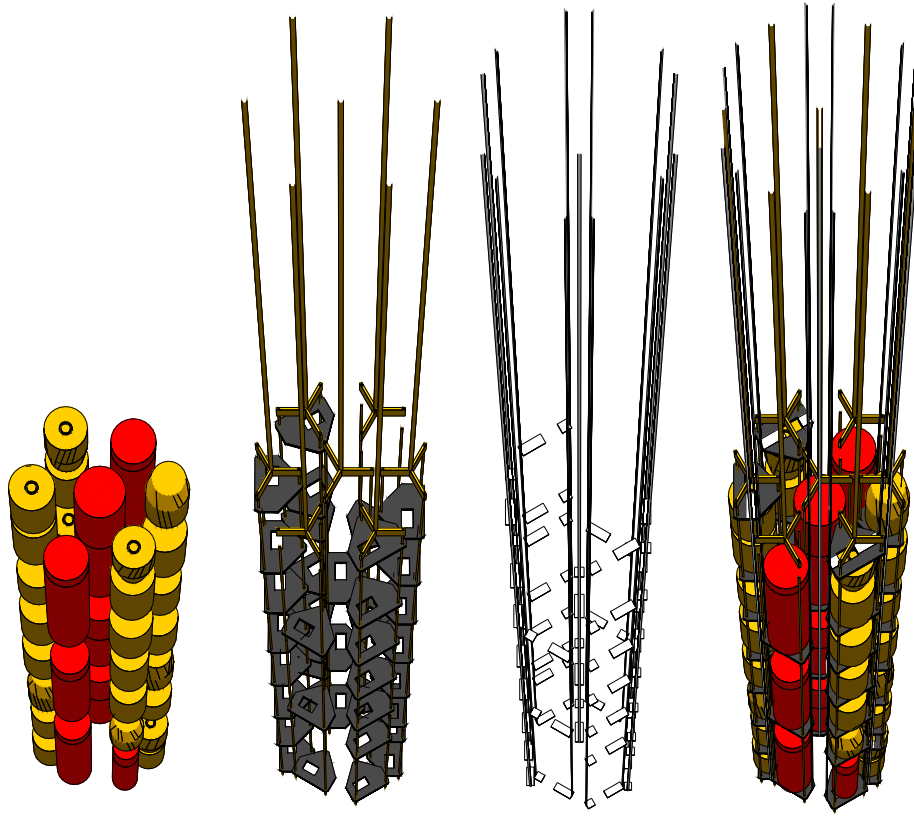


Figure 8: Implementation of the simulated volumes in MAGE. From left to right: the germanium detectors, the holder mounting, the cables and the three volumes put together.

Screening measurements revealed that contaminations with ^{40}K , one of the largest sources of natural radioactivity on Earth together with ^{238}U and ^{232}Th , are expected in the holder mounting, in the cables, in the mini-shroud and in the fiber-shroud. The four simulated spectra are shown in Fig. 10, top right.

^{42}Ar While the distribution of ^{42}Ar is homogeneous inside LAr, the short lived ionized decay product ^{42}K ($T_{1/2} = 12.3$ h) can have a significantly different distribution due to drifts of the ^{42}K ions inside the electric fields that are present near the detectors. Separate spectra for two ^{42}K distributions have thus been simulated: homogeneous in LAr in a volume of 17.7 m^3 centered around the full detector array, on the n^+ and on the p^+ detector surface of the detectors. As the spectral shape is not expected to vary strongly between the detectors, the isotope on the n^+ and p^+ surface was simulated only for a single detector. The simulated spectral shapes are shown in Fig. 10, bottom left.

^{238}U -CHAIN ^{214}Bi and ^{214}Pb are the only one in the $^{226}\text{Ra} \rightarrow ^{210}\text{Pb}$ sub-chain decaying by β -decay accompanied by emission of high energy γ particles and they are assumed to be in equilibrium. ^{214}Bi and ^{214}Pb were simulated in the holder mounting, in the cables, in the fiber-shroud and in the mini-shrouds (Fig. 10, bottom left). For the $^{238}\text{U} \rightarrow ^{226}\text{Ra}$ only the $^{234\text{m}}\text{Pa}$ was simulated (Fig. 11, top right), as the Q_β of ^{234}Th is below the considered

fitting range. The entire ^{238}U Decay chain is shown in Fig. 12, right.

The characteristic γ line at 2615 keV, a hint of the presence of isotopes from the ^{232}Th chain, can be clearly identified in the energy spectra shown in Fig. 9. Possible locations for contaminations are the detector assembly, the cables, the mini-shrouds and the fiber-shroud. As ^{228}Ac and ^{228}Th do not necessarily have to be in equilibrium, the two parts of the decay chain were simulated separately. From the sub-decay chain following the ^{228}Th decay only the contributions from the ^{212}Bi and ^{208}Tl β -decays were simulated (Fig. 11, top left), as these are the only ones emitting high energetic γ rays and electrons that can reach the detectors. The simulated ^{228}Ac spectrum is shown in Fig. 11, top right. The entire ^{232}Th Decay chain is shown in Fig. 12.

The presence of ^{60}Co in the holder mounting and ^{207}Bi was suggested by material screening measurements and earlier works (unpublished). Simulations of ^{60}Co in the holder mounting and ^{207}Bi in cables, holders and mini-shrouds have been carried out (see Fig. 11, top right).

From energies above 3.5 MeV the spectrum is dominated by α -decay events, thus the background model in this region has been developed independently and then the resulting energy distribution has been added as a single contribution among the other background contributions.

A strong contribution from ^{210}Po can be observed in Fig. 9. This is an indication for a surface contamination of the detectors. However, there are also hints for other peak like structures at 4.7, 5.4 and 5.9 MeV that can be attributed to the decays of ^{226}Ra , ^{222}Rn and ^{218}Po on p^+ detectors surfaces, respectively.

Due to the short range of α -particles in germanium and LAr of the order of tens of μm , only decays occurring on or in the close vicinity (few μm) of the p^+ surface (assumed p^+ dead layer thickness roughly 600 nm) can contribute to the measured energy spectrum as the n^+ dead layer thickness is roughly 1 mm. The energy deposited in the active volume of the detector by surface or close to surface α -particles is very sensitive to the thickness of the dead layer and on the distance of the decaying nucleus from the detector surface.

All α -decays in the ^{226}Ra to ^{210}Pb sub-decay chain and the ^{210}Po decay have been simulated on the p^+ detector surface separately. Additionally, the decays in the chain following the ^{226}Ra decay were simulated assuming a homogeneous distribution in a volume extending up to 1 mm from the p^+ surface in LAr. The individual decays on the p^+ surface result in a peak-like structure with its maximum at slightly lower energies than the corresponding α -decay energy with a quasi-exponential tail towards lower energy. The decays occurring in LAr close to the p^+ surface result in a quasi-flat spectrum without any peak-like structure extending to lower energies.

The ^{210}Po peak structure around 5.3 MeV with high statistics was used to determine the effective dead layer model. Spectra from ^{210}Po α -decay simulations on the p^+ surface with different dead layer thicknesses were used to fit the spectrum in the energy region dominated by the ^{210}Po peak, i.e. between 4850 and 5250 keV. The weight of each spectrum was left as a free parameter. A combination of the spectra for 500, 600 and 700 nm dead layer thicknesses describes the observed peak structure well and results in a good fit, whereas a spectrum with a single dead layer thickness does not give a sufficiently good fit. Consequently the derived dead layer model was used for the later fits of α -induced

^{232}Th -CHAIN

^{60}Co AND ^{207}Bi

α -MODEL

Table 5: Summary of the Monte Carlo simulations for the background model.

	Holders	Cables	Mini-shroud	Fibers	Contacts	LAr	Ge
$2\nu\beta\beta$							✓
$2\nu\beta\beta$ LV							✓
^{42}K					✓	✓	
^{40}K		✓	✓	✓	✓		
^{214}Bi	✓	✓	✓	✓			
^{214}Pb	✓	✓	✓	✓			
^{234m}Pa	✓		✓		✓		
^{212}Bi	✓	✓	✓	✓			
^{208}Tl	✓	✓	✓	✓			
^{228}Ac	✓						
^{60}Co	✓						
^{207}Bi	✓	✓	✓				
α -model							✓

spectra.

In order to describe the whole energy interval dominated by α -induced events, the simulated spectra of α -decays of ^{210}Po as well as from ^{226}Ra and its short lived daughter nuclei on the p^+ surface and in LAr were used to fit the energy spectrum between 3500 and 7500 keV. In fact, while the surface decays alone can successfully describe the observed peak structures, they could not describe the whole spectrum. A contribution from an approximately flat component, like the spectra from α -decays in LAr, is needed in the model. The number of events in the considered energy range was left as a free parameter for each α -component. The final spectra for BEGe and coaxial detectors are shown in Fig. 11, bottom left.

OTHER

The expected background indices due to the neutron and muon fluxes at the LNGS underground laboratory have been estimated to be of the order $< 10^{-5}$ cts/(keV·kg·yr) [49] and $< 10^{-4}$ cts/(keV·kg·yr) [50] respectively, and thus negligible. It has been also shown in earlier works that the contributions of the cryostat and water tank components are of the order $< 10^{-4}$ cts/(keV·kg·yr) [51], and likewise have not been considered in this analysis.

A summary of the background sources, along with their position, carried out for this analysis is given in Tab. 5.

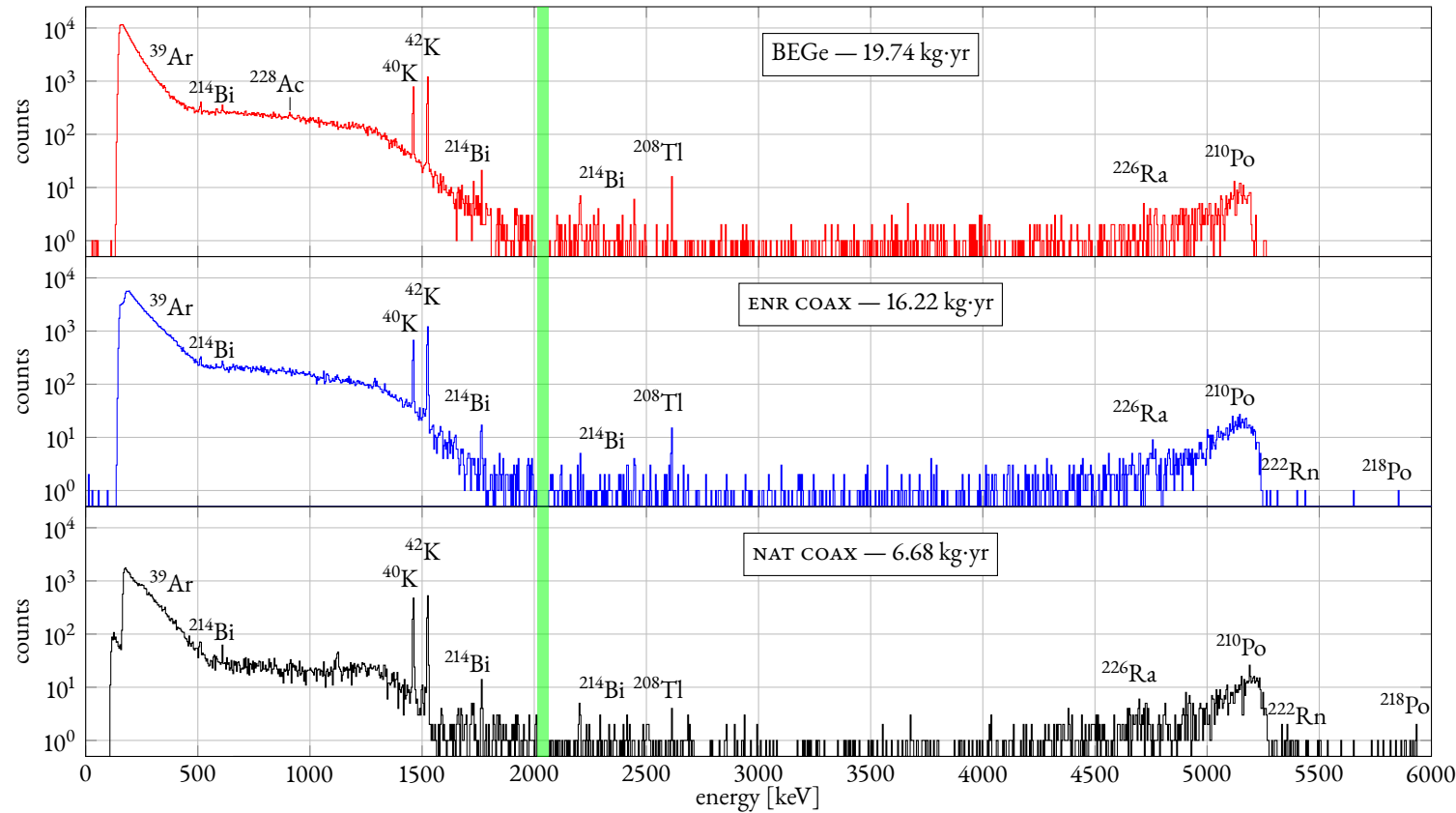


Figure 9: The summed energy spectrum (counts in logarithmic scale), showed separately for BEGe, enriched coaxial and natural coaxial detectors, produced using data from GERDA Phase II. The isotopes responsible for the relevant lines are reported on the plots together with the exposure. All the counts with energy greater than 3 MeV can be associated to α -events on the p^+ electrode. The blinding window $[Q_{\beta\beta} - 25 \text{ keV}, Q_{\beta\beta} + 25 \text{ keV}]$ is also shown in green. A 4 keV binning is adopted.

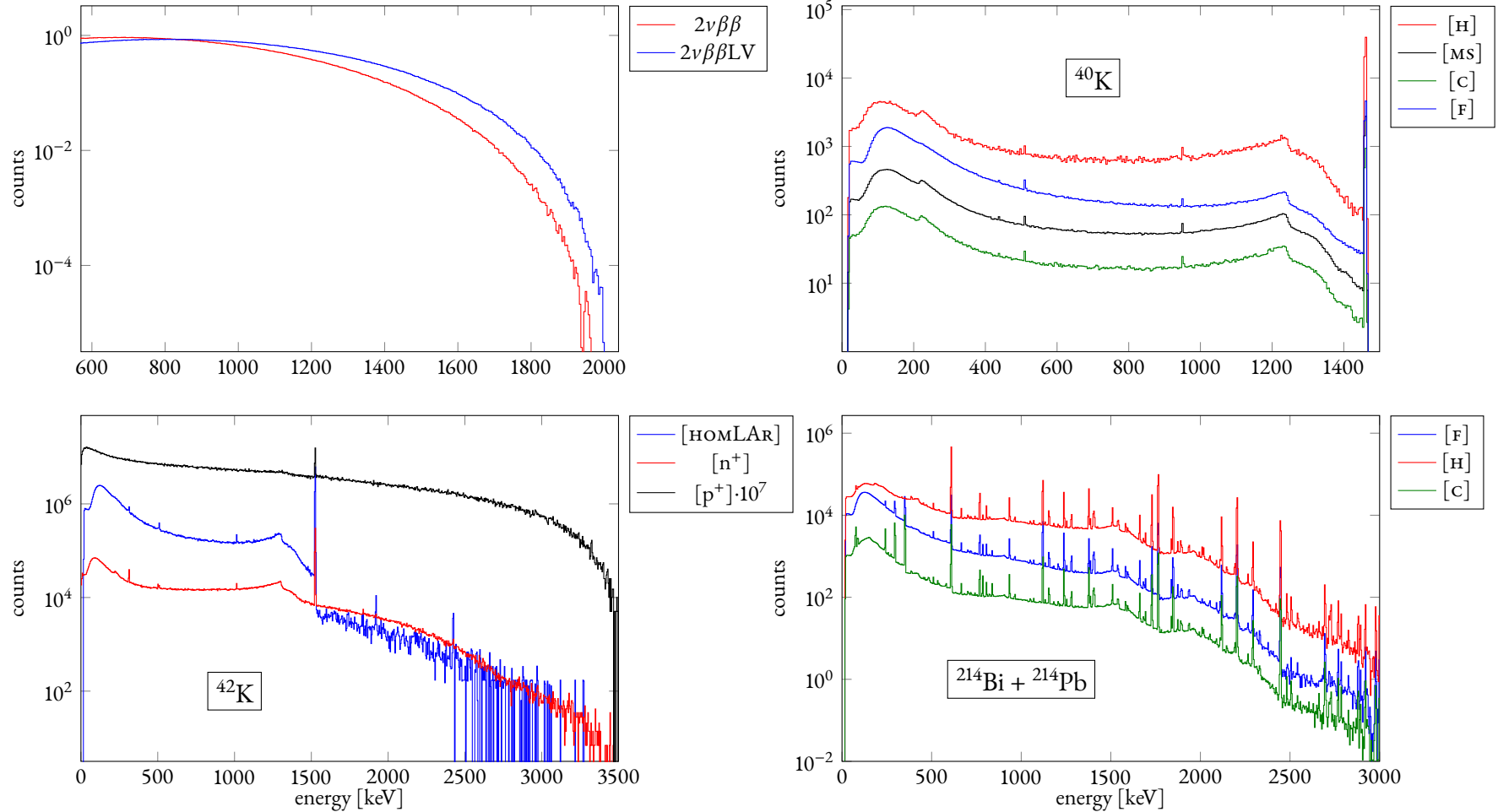


Figure 10: Simulated spectra, normalized to activity = 1 Bq/kg (except for $2\nu\beta\beta$), as described in §4. All spectra refer to BEGe detectors. Legend: [MS] = mini-shroud, [C] = cables, [H] = holders, [F] = fiber-shroud, [HOMLAR] = homogeneous in LAr, $[\text{n}^+]/[\text{p}^+]$ = contacts. Top left: the Standard Model and Lorentz-violating double-beta decay modes; top right: ^{40}K ; bottom left: ^{42}K ; bottom right: $^{214}\text{Bi} + ^{214}\text{Pb}$ summed spectra.

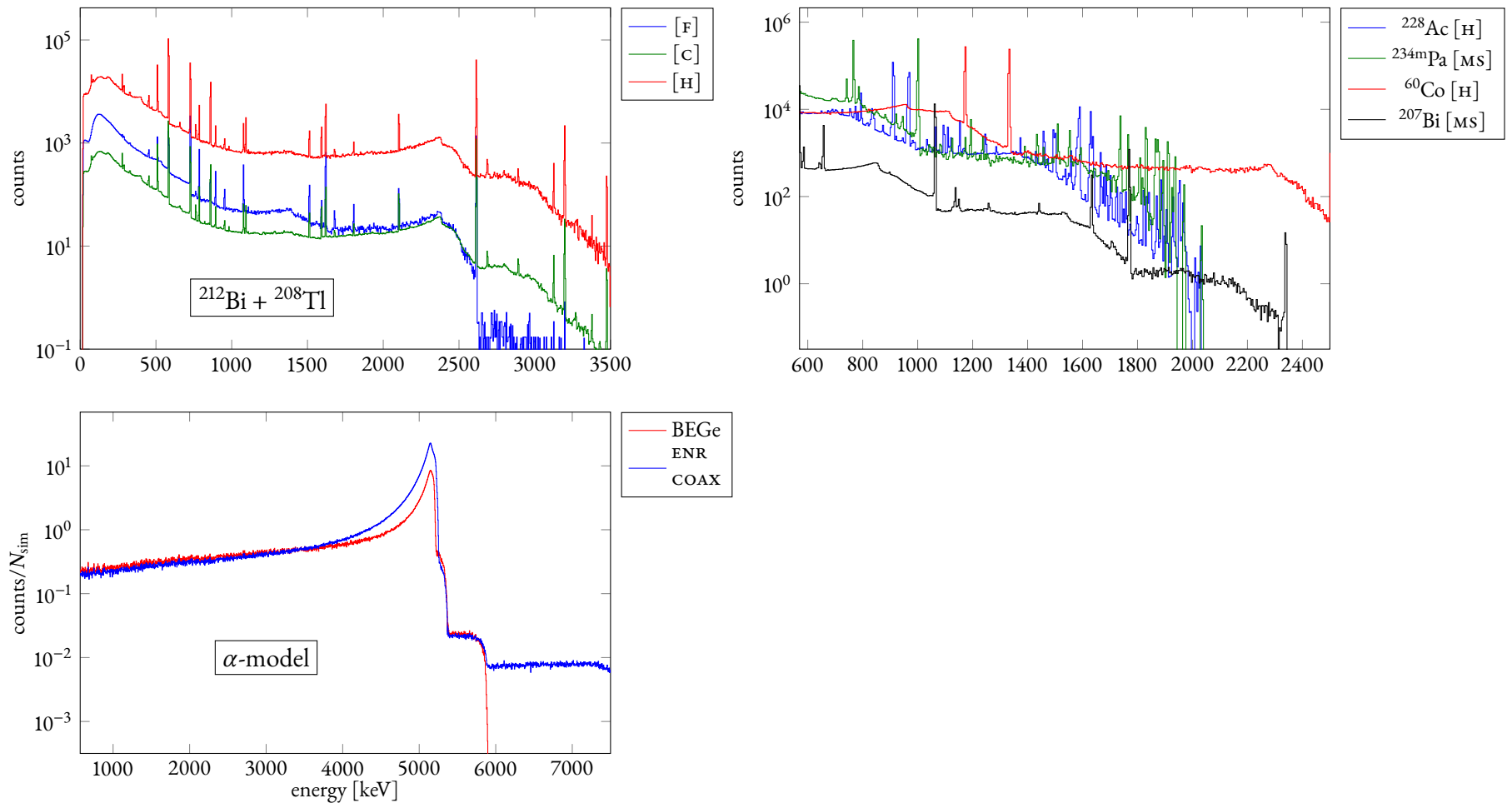


Figure 11: Simulated spectra, normalized to activity = 1 Bq/kg, as described in §4, except for the α -model which is simply normalized to the number of generated events. All spectra refer to BEGe detectors. Legend: [ms] = mini-shroud, [c] = cables, [h] = holders, [f] = fiber-shroud. Top left: ^{212}Bi and ^{208}Tl summed spectra; top right: ^{60}Co , ^{228}Ac , $^{234\text{m}}\text{Pa}$ and ^{207}Bi ; bottom left: α -model.

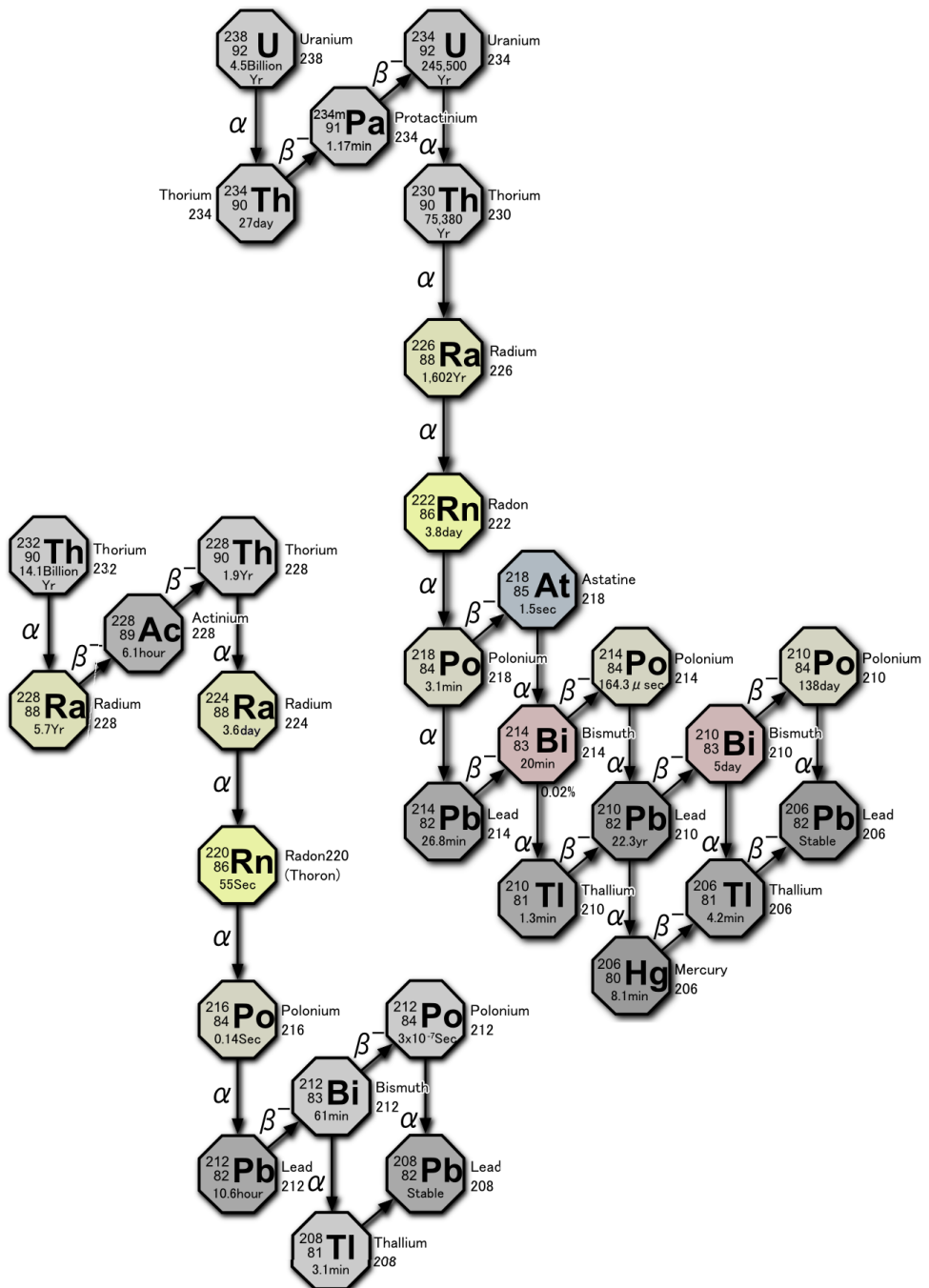


Figure 12: Schemes of ^{238}U and ^{232}Th decay chains.

4 Statistical analysis

A global model that describes the background spectrum was obtained by fitting the simulated spectra of different contributions to the measured energy spectrum using a Bayesian fit. A detailed description of the statistical method is given in the following.

A Bayesian approach

The gist of Bayesian statistics is not difficult to grasp. At its base there is the intuitive idea that probability quantifies the ‘degree of belief’ in an event. The probability of an event changes if other events are assumed to be ‘true’, provided these other events are ‘stochastically dependent’ on that event. This is the essence of Bayes’ theorem. As a consequence, Bayesian statistics allows the probability of a hypothesis to be continually updated on the basis of new observation (events) that depend on that hypothesis.

The theory or model can be used to provide ‘direct probabilities’; i.e., relative frequencies of possible outcomes of the results if an experiment is reproduced many times under identical conditions. The function $g(\vec{y} \mid \vec{\lambda}, M)$ gives the relative frequency of getting results \vec{y} assuming the model M and parameters $\vec{\lambda}$. It should satisfy

$$\int g(\vec{y} \mid \vec{\lambda}, M) d\vec{y} = 1 \quad \text{and} \quad g(\vec{y} \mid \vec{\lambda}, M) > 0 \quad (16)$$

if continuous values are measured (in the discrete situation the integral gets replaced by a sum over all the possible outcomes). In the following, we will write formulae for the continuous case; the modification for the discrete case will be clear.

The prediction \vec{y} from the model cannot usually be directly compared to the experimental results (that we will denote with \vec{x} in the latter), the modeling of the experiment will usually add extra parameters and assumptions. We will use the symbol \vec{v} to represent these additional nuisance parameters, which could also be limited by additional information not included explicitly in the model. In the following we will implicitly assume that all available information is used in the probability distributions. We would then have $f(\vec{x} \mid \vec{\lambda}, \vec{v}, M)$ for the frequency distribution of the experimentally observable quantities \vec{x} .

In general, the judgement on the validity on a model and the extraction of values of the parameters within the model will be based on a comparison of the data \vec{D} with $f(\vec{x} \mid \vec{\lambda}, \vec{v}, M)$.

The probability of a model M will be quantified as $P(M) \in [0, 1]$, while the probability density of the parameters are typically continuous functions. The parameters from the modeling of the experimental conditions are not correlated to the parameters of the physical model so that

$$P(\vec{\lambda}, \vec{v} \mid M) = P(\vec{\lambda} \mid M)P(\vec{v}) . \quad (17)$$

THE
LEARNING
RULE

In the Bayesian approach the quantities $P(M)$, $P(\vec{\lambda} \mid M)$ etc. are treated as probabilities (probability densities), although they are not in any sense frequency distributions and

are more accurately described as *degrees-of-belief* [52]. The *degree-of-belief* contains our knowledge about nature and has to be ‘updated’ by comparing data with the predictions of the model.

The procedure for learning from experiment is, according to the Bayes theorem:

$$P_{i+1}(\vec{\lambda}, \vec{v}, M | \vec{D}) = \frac{f(\vec{x} = \vec{D} | \vec{\lambda}, \vec{v}, M) P_i(\vec{\lambda}, \vec{v}, M)}{\sum_M f(\vec{x} = \vec{D} | \vec{\lambda}, \vec{v}, M) P_i(\vec{\lambda}, \vec{v}, M)}, \quad (18)$$

where the index on P represents the state-of-knowledge that gets updated from i to $i + 1$. P_i is called *prior* probability and P_{i+1} is subsequently called *posterior* probability. The normalization factor derives from the normalization requirements on P and we can also write it as $P(\vec{D})$, the probability to get the data \vec{D} .

For a given model M , f is a function of the model parameters, the experimental parameters, and the possible outcomes \vec{x} . When f is viewed as a function of $(\vec{\lambda}, \vec{v})$ for fixed $\vec{x} = \vec{D}$, it is known as the *Likelihood*. If f is normalized, we can write

$$P(\vec{D} | \vec{\lambda}, \vec{v}, M) = f(\vec{x} = \vec{D} | \vec{\lambda}, \vec{v}, M). \quad (19)$$

THE ROLE OF PRIORS

The presence of the prior distribution $P(\vec{\lambda}, \vec{v}, M)$ could generate suspects upon the ‘objectivity’ of the statistical analysis, in the sense that scientific conclusions may depend on ‘prejudices’ about the value of a physical quantity. This is a logical necessity of the Bayesian approach, in which those who have done the experiment are the natural candidates to turn Likelihoods in probabilistic statements.

At an intuitive level, it is absolutely reasonable to draw conclusions starting from some prior knowledge, rather than in a purely automatic way. For example, in the most extreme case, if the experimental information is scarce or doubtful it is absolutely right to believe more in personal prejudices than in empirical data. Moreover, if different observers have priors which are so different that they reach divergent conclusions, it just means that the data is still not sufficiently solid to allow a high degree of intersubjectivity and we are on a sticky ground. Thus, one is expected to use different prior distributions to test the robustness of his probability statements [52].

PARAMETER ESTIMATION

Parameter estimation is performed while keeping the model fixed. In this case we write

$$P(\vec{\lambda}, \vec{v} | \vec{D}, M) = \frac{P(\vec{x} = \vec{D} | \vec{\lambda}, \vec{v}, M) P_0(\vec{\lambda}, \vec{v} | M)}{\int P(\vec{x} = \vec{D} | \vec{\lambda}, \vec{v}, M) P_0(\vec{\lambda}, \vec{v} | M)}, \quad (20)$$

where the prior distribution is now denoted with P_0 . The output of the evaluation is a normalized probability density for the parameters, including all correlations, and hence it can be used to give best-fit values, probability intervals for the parameters, etc.

When working with the posterior probability density function (or *pdf*) (20), it is often the case that one is interested not in the full *pdf*, but in the probability distribution for only one, or a few, parameters. These distributions are determined via marginalization. For example, the probability distribution for parameter λ_i is:

$$P(\lambda_i | \vec{D}, M) = \int P(\vec{\lambda}, \vec{v} | \vec{D}, M) d\vec{\lambda}_{i \neq j} d\vec{v}. \quad (21)$$

Note that the parameter values which maximize the full posterior *pdf* usually do not coincide with the values which maximize the marginalized distributions.

We will mainly interested in estimating the mode of λ_i , i.e. the value of λ_i which maximizes the marginalized posterior *pdf*

$$\operatorname{argmax} \left[P(\lambda_i | \vec{D}, M) \right] \quad (22)$$

and confidence intervals such that a certain fraction α of the total area is contained in it:

$$\alpha = \int_{\lambda_{\text{lower}}}^{\lambda_{\text{upper}}} P(\lambda_i | \vec{D}, M) d\lambda_i, \quad (23)$$

where the desired interval is $[\lambda_{\text{lower}}, \lambda_{\text{upper}}]$.

Model testing in a strictly Bayesian approach is problematic since there is often no way to define all possible models, and the results depend critically on the choice of priors. However, having a number representing how well the model fits the available data is important. Here we consider a p-value that gives a goodness-of-fit criterion based on the ‘likelihood’ of the data in the model under consideration using the parameters defined at the mode of the posterior. We define the following function:

$$\hat{f}(\vec{x}) = P(\vec{x} | \hat{\vec{\lambda}}, \hat{\vec{\nu}}, M), \quad (24)$$

where $(\hat{\vec{\lambda}}, \hat{\vec{\nu}})$ is the set of parameters at the mode of the full *pdf*. We then define the p-value as

$$p = \frac{\int_{\hat{f}(\vec{x}) < \hat{f}(\vec{D})} \hat{f}(\vec{x}) d\vec{x}}{\int \hat{f}(\vec{x}) d\vec{x}}. \quad (25)$$

p is the tail area probability to have found a result with $\hat{f}(\vec{x}) < \hat{f}(\vec{D})$, assuming that the model M is valid and all experimental effects are perfectly known. It is the probability that the Likelihood could have been lower than the observed in the data, so if the model does not give a good representation of the data, then p will be a small number. If the modeling is correct, p will have a flat probability distribution in $[0, 1]$, but it should be clear that incorrect formulations of the data fluctuations will bias the p-value distribution to lower (if the data fluctuations are underestimated) or higher (if the data fluctuations are overestimated) values. Also, if the existing data is used to modify the parameter values, the extracted p-value will be biased to higher values.

One should also keep in mind that p-values cannot be turned into probabilistic statements about the model being correct without priors, and should therefore be handled with care. General guidelines suggest that one should check if the p-value distribution is reasonably flat, keeping in mind that sharply falling distributions starting at $p = 0$ are usually originated by a bad model. Moreover, small p-values are worrisome, they indicate that a poor model might has been picked. For further discussions on the topic see, for example, [53].

MODEL
VALIDITY

COMPUTATIONAL
ASPECTS

There are several ways to calculate the posterior in 20 and the marginalized *pdf*s, and even with few parameters ($\vec{\lambda}, \vec{v}$) the computation can easily become highly time consuming. However, the application of Markov Chain Monte Carlo (MCMC) methods in this field has revolutionized Bayesian computation. The BAT package [54] implements several tools to perform a Bayesian data analysis.

Markov chains are sequences of random numbers (or, in general, vectors of numbers), X_t , which follow a well-defined limiting distribution, $\pi(x)$. The fundamental property of a Markov chain is that the probability distribution for the next element in the sequence, X_{t+1} , depends only on the current state, and not on any previous history. A Markov chain is completely defined by the one-step probability transition matrix, $P(X_{t+1} | X_t)$. Under certain conditions (recurrence, irreducibility, aperiodicity), it can be proven that the chain is ergodic; i.e., that the limiting probability to be in a given state does not depend on the starting point of the chain. An MCMC is an algorithm producing an ergodic Markov chain whose stationary distribution is the distribution of interest. In our case, the BAT package produces a Markov chain where the stationary distribution is the desired posterior *pdf*.

A very popular algorithm that achieves this is the Metropolis-Hastings algorithm [55, 56]. The algorithm works as follows:

1. Given the system in a starting state $X_t = \vec{x}$, a new proposed state \vec{y} is generated according to a symmetric proposal function $g(\vec{y}, \vec{x})$ (in our application a state is a set of parameter values);
2. The Hastings test ratio

$$r = \min \left[1, \frac{\pi(\vec{y})}{\pi(\vec{x})} \right]$$

is calculated, and then the generated state \vec{y} is accepted or rejected with probability r , i.e.:

- (a) A random number u is generated from a uniform distribution between 0 and 1, $\text{Unif}[0, 1]$;
- (b) If $u < r$ $X_{t+1} = \vec{y}$ is set, else $X_{t+1} = \vec{x}$ is taken.

It is possible to show that, given a reasonable proposal function g , this algorithm satisfies the conditions of an MCMC, and that the limiting distribution is $\pi(\vec{x})$. Thus this allows for the production of states distributed according to the desired distribution.

IMPLEMENTATION

The BAT software is C++ based code interfaced to software packages such as ROOT [37], MINUIT [57], or the CUBA library [58]. Several Markov chains can optionally be run in parallel thanks to the OpenMP [59] support. For further details about theoretical and implementation aspects, as well as applications to real problems, underlying the BAT package see [54]. For a detailed description of the class structure and the methods the official documentation is available at <http://www.mppmu.mpg.de/bat/>.

Background decomposition

The analysis of the energy distributions was carried out by fitting binned energy distributions. The Likelihood $P(\vec{D} | \vec{\lambda})$ is written as the product of the probability of the data given the model and parameters in each bin:

$$P(\vec{D} | \vec{\lambda}) = \prod_i^N P(n_i | \mu_i) = \prod_i^N \frac{e^{-\mu_i} \mu_i^{n_i}}{n_i!}, \quad (26)$$

where N is the number of bins, n_i is the observed number of events and μ_i is the expected number of events (frequency) in bin i . μ_i can be written as the sum of the background contributions in bin i :

$$\mu^i = \sum_j b_j^i = \sum_j c_j h_j^i, \quad (27)$$

where the index j runs over all the background contributions and b_j^i is the expected number of events for the background source j in bin i . The latter can be further decomposed in the product of the frequency h_j^i in bin i and a factor c_j , which does not depend on the bin and contains the λ_j parameter of physical interest that will be estimated with the fitting procedure.

We want to keep the summed energy spectra from BEGe and coaxial detectors separate, as the contamination of radioactive sources on the electrodes can be different. All the other parameters (e.g. the double-beta decay half-life or the ^{60}Co activity in the detector assembly) are the same for the two spectra. The natural coaxial detectors are omitted from the analysis because the contribution to the double-beta decay spectrum is too small to be relevant. Then the Likelihood can be expressed as

$$P(\vec{D} | \vec{\lambda}) = P_{\text{BEGe}}(\vec{D} | \vec{\lambda}) P_{\text{COAX}}(\vec{D} | \vec{\lambda}) = \prod_i^N \left[\frac{e^{-\mu_i} \mu_i^{n_i}}{n_i!} \right]_{\text{BEGe}} \prod_j^N \left[\frac{e^{-\mu_j} \mu_j^{n_j}}{n_j!} \right]_{\text{COAX}} \quad (28)$$

For the two-neutrino mode of double-beta decay we want to estimate the half-life $2\nu\beta\beta T_{1/2}^{2\nu}$. In this case the contribution $b_{2\nu}^i$ can be written as

$$b_{2\nu}^i = \frac{N_A \log 2}{A_{76} T_{1/2}^{2\nu}} \sum_{k=1}^{\text{DET}} m_k t_k f_k^{76} [\varepsilon_{2\nu}^i f^i]_{2\nu}, \quad (29)$$

where k labels the detectors, N_A is the Avogadro number, A_{76} is the molar weight of ^{76}Ge , f^{76} is the enrichment fraction, and t is the detector's live time. The detection efficiency $\varepsilon_{2\nu}^{ik}$ has to be intended as a generalized efficiency which comprises the effect of the presence of the dead layer and the intrinsic efficiency of the detector k . $f_{2\nu}^i$ is the theoretical absolute frequency for double-beta decay in bin i (i.e. the discrete version of (7)). We have assumed $T_{1/2}^{2\nu} \gg t$.

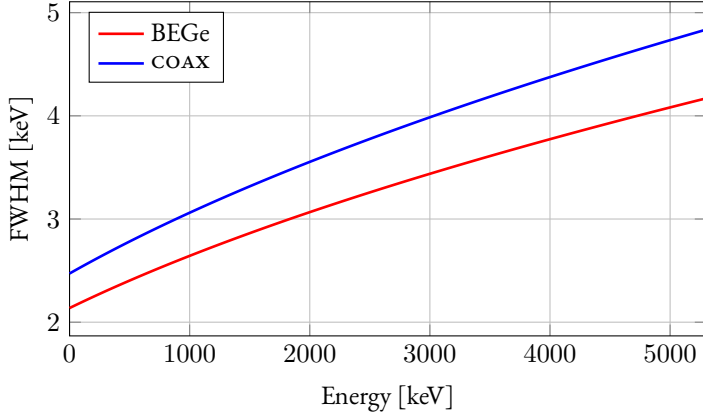


Figure 13: Combined resolution curves for the BEGes (red) and enriched coaxials (blue) detectors.

The expression holds also for the Lorentz-violating mode, with the associated half-life $T_{1/2}^{2\nu\text{LV}}$. Recalling Eq. (12) we can express $T_{1/2}^{2\nu\text{LV}}$ in relation to $T_{1/2}^{2\nu}$ and $\dot{a}_{\text{of}}^{(3)}$:

$$T_{1/2}^{2\nu\text{LV}} = I \cdot \frac{T_{1/2}^{2\nu}}{\dot{a}_{\text{of}}^{(3)}}, \quad I = \frac{10}{\dot{a}_{\text{of}}^{(3)}} \frac{\int_0^{K_0} \frac{d\delta\Gamma}{dK} dK}{\int_0^{K_0} \frac{d\Gamma_0}{dK} dK}, \quad (30)$$

and then the $b_{2\nu\text{LV}}^i$ factor can be written as:

$$b_{2\nu\text{LV}}^i = \frac{\dot{a}_{\text{of}}^{(3)}}{I} \frac{N_A \log 2}{A_{76} T_{1/2}^{2\nu}} \sum_{k=1}^{\text{DET}} m_k t_k f_k^{76} [\varepsilon_k^i f_j^i]_{2\nu\text{LV}}. \quad (31)$$

EXTERNAL SOURCES For the other background sources the parameter of interest is the activity, defined as the number of events per unit of time and mass. Assuming a stable isotope contamination within the considered live times, we can express b_j as

$$b_j^i = a_j M \sum_k t_k \varepsilon_j^{ik} f_j^i, \quad (32)$$

where a_j is the activity for the source j and M is the mass of the object in which the source is located. The detection efficiency ε_j^{ik} has to be intended as a generalized efficiency which comprises the effect of the presence of the dead layer, the intrinsic efficiency and the solid angle the detector k subtends at the radioactive source. f_j^i is the theoretical frequency of the energy outcomes for source j in bin i .

SIMULATED SPECTRA The simulated spectra for $2\nu\beta\beta$ and background sources, come from MAGE in the form

$$b_{\text{MAGE},j}^{ik} = N_{\text{gen}} \varepsilon_j^{ik} f_j^i, \quad (33)$$

where N_{gen} is the number of primary vertices simulated and i, j, k label the i -th bin, the source and the detector, respectively.

First of all the experimental energy resolution has to be applied to the spectra with a convolution between the latter and the ‘resolution curves’. They were estimated using ^{228}Th sources deployed into LAr and are represented by a square-root-like function. For the present analysis we used two different global calibration curves: one for the BEGes and one for the enriched coaxials (Fig. 13), as the differences between the single curves within the two detector’s types are negligible.

The spectra for each detector have then to be combined properly in order to be fitted to the data. In the case of external sources, for example, the Eq. (32) has to be reproduced rescaling each spectra with N_{gen} , then multiplying by t_k and M and finally summing over all detectors. Then the overall factor λ_i will be the parameter to estimate with the fitting procedure:

$$b_{\text{fit},j}^i = \lambda_j M \sum_k^{\text{DET}} t_k \varepsilon_j^{ik} f_j^i . \quad (34)$$

5 Results

The analysis covers the range of data collected between December 2015 and March 2017, namely from Run53 to Run79, excluding Run66 and Run68, in the GERDA nomenclature. This corresponds to an exposure of 19.74 kg·yr for the BEGes and 16.22 kg·yr for the enriched coaxials. As mentioned in the previous chapters, data from natural coaxial detectors is not considered in this analysis, as the contribution to the $2\nu\beta\beta$ spectrum is negligible. Due to the presence of the blinding window data corresponding to an energy deposition that lies within ± 25 keV around the $Q_{\beta\beta}$ is neglected in the Likelihood computation.

The fit range was optimized to include the largest subset of data possible. The lower limit was set just above the ${}^{39}\text{Ar}$ Q-value, corresponding to 570 keV, because of three factors: the scarce knowledge of the contributions to the background spectra in that region, the relatively large uncertainty on the dead layer thickness in the coaxial detectors that strongly affects the low energy region and finally the uncertainties related to the performance of the energy threshold of the acquisition trigger. The upper limit was set to 5.3 MeV to include the α -region and better constrain the contribution of the α -model in the $2\nu\beta\beta$ region.

P-VALUE COMPUTATION According to Eq. (25), One should compute the integral of the complete posterior distribution in order to evaluate the p-value. However, despite the powerful numerical integration tools shipped with BAT, the calculation fails if the parameter space dimension is approximatively greater than 10, as in the case of such a rich set of background sources. Anyway, instead of trying to solve a hard numerical problem, one can adopt a different approach applying again the MCMC methods, as suggested in [53]. With a data set probability modeled as a product of Poisson terms, as the case of fitting histograms, the highest probability occurs when each bin's content matches the theoretical prediction. We used the best-fit energy histogram to define the starting point for a Markov chain. Moving the bin contents randomly up or down and applying the usual Metropolis test a large number of experiments can be quickly simulated and the p-value extracted.

BINNING At the beginning, data was binned with a fixed-size 4 keV binning. Then, at a first glance to results, it was realised that there was a great discrepancy between the model and data around the visible γ -lines of ${}^{40}\text{K}$ and ${}^{42}\text{K}$ and then the p-value was very low. This is always the case when dealing with γ -lines split over two or three bins, where the reliability of the energy calibration and resolution curves is essential. Thus, a variable binning that takes into account this effect has been adopted. Bins containing the most visible γ -lines in data have been merged into one, in particular: the ${}^{42}\text{K}$ line at 1461 keV, the ${}^{40}\text{K}$ line at 1525 keV, the ${}^{208}\text{Tl}$ line at 2614 keV, and the ${}^{214}\text{Bi}$ lines at 609, 1764, 2204 and 2447 keV. A summary of the binning sizes is given in Tab. 6.

PRIORS For the $2\nu\beta\beta$ half-life $T_{1/2}^{2\nu}$ two prior distributions have been considered: a flat one between 1.74 and $2.09 \cdot 10^{21}$ yr, corresponding to $\propto 1/y^2$ when fitting $y = 1/T_{1/2}^{2\nu}$, and a gaussian one centered on the result of GERDA Phase I [60]:

$$(1.926 \pm 0.095) \cdot 10^{21} \text{ yr}, \quad (35)$$

Table 6: Bin sizes adopted in the considered energy range.

Source	Line [keV]	bin size [keV]
^{42}K	1461	12
^{40}K	1525	12
^{208}Tl	2614	12
	609	12
^{214}Bi	1764	8
	2204	8
	2247	12
else		4

with a σ equal to the quoted error. When fitting $y = 1/T_{1/2}^{2\nu}$, this corresponds to a prior:

$$\propto \frac{1}{y^2} \exp\left[-\frac{\left(\frac{1}{y} - \mu\right)^2}{2\sigma^2}\right].$$

The two priors are shown in Fig. 14 in blue.

Some of the results from the screening measurements of the materials, reported in Tab. 4, have been used to set prior distributions on the background activities. A gaussian prior is set when a precise activity with error is specified, a flat distribution is set when only an upper limit, or no information, is available. A special treatment is applied for measurements concerning cable activities. In GERDA, four types of cables are used to transport signals and provide power supply, but only three of them were screened to study their radioactivity. Furthermore there are some specific cables that come from a separate batch that were not screened too. Thus, it has been decided not to use the available results to set priors but only to provide a post-analysis consistency check to the activities in the MAGE volume for the cables given by the fit. Activities from the three cable types reported in Tab. 4 were combined as follows: they were weighted considering their actual presence in terms of mass in GERDA. For the non-screened cable type, Tecnomec 2 mils, the same specific contamination of Tecnomec 3 mils was assumed.

Standard Model double-beta decay mode

In a first approach in studying the background model only the standard mode of $2\nu\beta\beta$ was included, in order to compare the results on the half-life with the one found in literature. The presence of all the background sources suggested by the screening measurements, plus the ^{207}Bi which is known to be present by other studies, was tested in a first fit model. Then the parameters showing an exponential decay as a marginalised posterior, thus with only an upper limit, were excluded one-by-one from the fit to gain in the end a minimal background model, which will be presented in the following.

**NON-INFORMATIVE
MODEL**

In this first analysis ‘non-informative’ prior distributions were set for all parameters, meaning that the prior distributions were taken to be uniform in the activities of the background sources and uniform in $T_{1/2}^{2\nu}$. The results with the minimal model and non-informative priors are given in Tab. 7. For each parameter the mode of the total posterior distribution (global mode) and the mode of the marginalised distribution (marginalised mode), together with the 1σ -contour of the marginalised distribution are given. The corresponding Background Index, where available, is also given separately for the summed BEGe detectors and for the summed enriched coaxial detectors. The posterior distribution of $1/T_{1/2}^{2\nu}$, together with its prior distribution uniform in $T_{1/2}^{2\nu}$ is shown in Fig. 14, right.

COMMENTS

One of the first notable things about these preliminary results is that the ${}^{40}\text{K}$ activity in the fiber-shroud is much greater than the expectations. In this component the result from material screening is three orders of magnitude less than the output of the fit, while on the holder mounting and on the cables the output is compatible with expectations. Actually, on the cables we can only extract an upper limit on the ${}^{40}\text{K}$ contamination, as the posterior distribution is peaked in zero and broadens exponentially towards largest values. This situation changes in the model with informative priors, as it will be shown later. It should be noted here that in all the tested configurations the fitting procedure rejected the hypothesis of a ${}^{40}\text{K}$ contamination in the mini-shroud. Summarizing, there is a clear indication of the presence of additional ${}^{40}\text{K}$ contaminations in components located far from the detector array, not indicated by the screening measurements. For all the other activities the results are compatible with expectations, where available. The result on $T_{1/2}^{2\nu}$, using the global mode as the central value and the 1σ -contour extracted from the marginalised posterior as the associated statistical error, is:

$$(1.993 \begin{array}{l} +0.022 \\ -0.021 \end{array}) \cdot 10^{21} \text{ yr}, \quad (36)$$

which is compatible with the GERDA Phase I result (35). A p-value of 0.93 strongly supports the reliability of this minimal background model.

**INFORMATIVE
MODEL**

After the first, non-informative, analysis the results from the material screening were used, where possible, to constrain the fitting procedure. From now on we will refer to this new model as the ‘informative’ model. The results on the ${}^{40}\text{K}$ activity on the fiber-shroud clearly indicates the inadequacy of the screening measurements to describe the actual contamination. Hence, only the gaussian prior distribution on the ${}^{40}\text{K}$ activity on the holder mounting has been added to the fit, as the result of the fit is compatible with the expectations. Then, a gaussian prior on the ${}^{212}\text{Bi} + {}^{208}\text{Tl}$ activity in the fiber-shroud and a gaussian prior on $T_{1/2}^{2\nu}$, centered on the GERDA Phase I result (35), have also been set. Results are given in Tab. 8, where the presence of an informative prior is marked with a (\dagger) near the name of the source.

COMMENTS

The first prominent feature of this informative model is a much lower value in the fiber-shroud and a higher one in the cables for the ${}^{212}\text{Bi} + {}^{208}\text{Tl}$ activity. This is a natural consequence of the introduction of a prior distribution on the ${}^{212}\text{Bi} + {}^{208}\text{Tl}$ activity in the fiber-shroud, which obliges the fit to move the additional activity in the cables. However, the p-value is substantially the same of the non-informative model, and the

Table 7: Results for the minimal background model with non-informative priors. The global and the marginalised mode, together with the 1σ -contour of the marginalised distribution are provided. The Background Index (BI), summed separately over BEGe and enriched coaxial detectors, is also given (the field is left blank when the Q-value of the background source is below the ROI). The units are mBq/kg if not specified after the source name. Upper limits are given at 90% C.I.

Source	Global [mBq/kg]	Marg. [mBq/kg]	1σ [mBq/kg]	BI[BEGe] [10^{-2} cts/(keV·kg·yr)]	BI[COAX]
$T_{1/2}^{2\nu}$ [10^{21} yr]	1.993	1.986	$+0.022$ -0.021	0.001	0.001
FIBERS					
^{40}K	94	88	$+13$ -15	–	–
$^{212}\text{Bi} + ^{208}\text{Tl}$	1.3	2.1	$+2.1$ -1.6	0.037	0.039
$^{214}\text{Pb} + ^{214}\text{Bi}$	1.58	2.07	$+0.63$ -0.77	0.131	0.149
HOLDERS					
^{40}K	4.8	2.1	$+2.1$ -1.9	–	–
$^{214}\text{Pb} + ^{214}\text{Bi}$	0.108	0.049	$+0.064$ -0.052	0.112	0.080
^{228}Ac	0.314	0.321	± 0.075	0.005	0.005
^{60}Co	0.110	0.098	± 0.025	0.056	0.045
CABLES					
^{40}K	–	< 300	–	–	–
$^{212}\text{Bi} + ^{208}\text{Tl}$	10.7	9.5	$+2.6$ -3.0	0.249	0.197
$^{234\text{m}}\text{Pa}$	7.0	5.7	$+4.3$ -3.8	0.002	0.003
MINI-SHROUD					
^{207}Bi	0.72	0.59	$+0.44$ -0.38	0.001	0.004
OTHER					
^{42}K in LAr	0.2004	0.2002	± 0.0038	0.380	0.474
^{42}K on COAX n ⁺ [cts]	570	630	± 170	–	0.324
α -model BEGe [cts]	1315	1332	± 50	0.406	–
α -model COAX [cts]	2960	2962	± 78	–	0.475
TOTAL				1.38 ± 0.63	1.80 ± 0.79
p-value					0.93

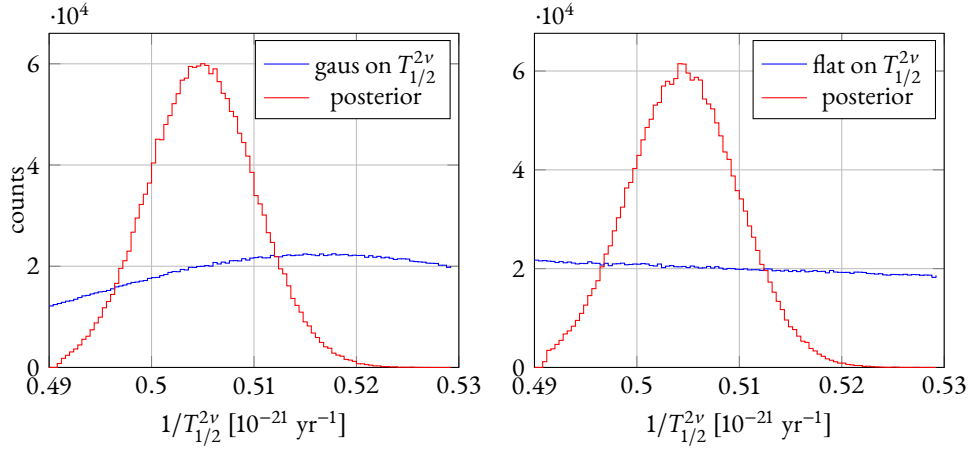


Figure 14: Prior and posterior distributions of $1/T_{1/2}^{2\nu}$. On the right: result with a uniform prior in $T_{1/2}^{2\nu}$, on the left: result with a gaussian prior in $T_{1/2}^{2\nu}$ centered on the GERDA Phase I result (35).

resulting activity on the cables is compatible with the expectations from the screening measurements, so we retained this model as valid. Also the prior setting on the ${}^{40}\text{K}$ activity in the holder mounting had some noticeable effects: the 1σ contour is reduced by a factor of two and the central value is less than the non-informative model. As a consequence, the ${}^{40}\text{K}$ activity on cables now has a definite value (even if with a large error), and not only an upper limit, because of the migration of events from the holder mounting. The value of $T_{1/2}^{2\nu}$ is found to be slightly reduced with respect to the non-informative model, although still inside the 1σ countour:

$$(1.984 \begin{array}{l} +0.020 \\ -0.020 \end{array}) \cdot 10^{21} \text{ yr}. \quad (37)$$

All the other results essentially remain the same as the non-informative model. The result of the background decomposition are plotted in terms of energy spectra for different energy ranges and for the two data sets, BEGe and enriched coaxial summed detectors, in Fig. from 17 to 30. In particular, in Fig. 29 and Fig. 30, the background contributions in the ROI are shown.

Systematic uncertainties

To give an estimate of the systematic error associated to the two-neutrino double-beta decay half-life various sources must be considered.

- ◊ First of all, the choice of the binning size could lead to a systematic error. To estimate the impact of the choice on the stability of $T_{1/2}^{2\nu}$ some meaningful values for the bin size have been considered, for which the analysis was repeated. Bin sizes below the currently used 4 keV value have not been considered because of the scarce reliability of the energy calibrations and of the energy resolution curves at

Table 8: Results for the minimal background model with informative priors. The global and the marginalised mode, together with the 1σ -contour of the marginalised distribution are provided. The Background Index (BI) summed separately over BEGe and enriched coaxial detectors is also given (the field is left blank when the Q-value of the background source is below the RoI). The presence of an underlying informative prior distribution is marked with (\dagger) .

Source	Global [mBq/kg]	Marg. [mBq/kg]	1σ [mBq/kg]	BI [BEGe] [10^{-2} cts/(keV·kg·yr)]	BI [COAX]
$T_{1/2}^{2\nu}$ [10^{21} yr] (\dagger)	1.984	1.980	± 0.020	0.001	0.001
FIBERS					
^{40}K	89.71	88.65	$^{+11}_{-14}$	–	–
$^{212}\text{Bi} + ^{208}\text{Tl}$ (\dagger)	0.0583	0.0595	± 0.012	0.002	0.002
$^{214}\text{Pb} + ^{214}\text{Bi}$	2.08	2.13	$^{+0.64}_{-0.77}$	0.149	0.169
HOLDERS					
^{40}K (\dagger)	4.00	4.17	0.83	–	–
$^{214}\text{Pb} + ^{214}\text{Bi}$	0.064	0.052	$^{+0.065}_{-0.052}$	0.086	0.062
^{228}Ac	0.315	0.305	± 0.075	0.005	0.005
^{60}Co	0.086	0.099	± 0.025	0.053	0.042
CABLES					
^{40}K	79	46	$^{+89}_{-63}$	–	–
$^{212}\text{Bi} + ^{208}\text{Tl}$	12.1	11.9	± 1.6	0.285	0.226
$^{234\text{m}}\text{Pa}$	7.2	6.0	$^{+4.3}_{-3.8}$	0.002	0.002
MINI-SHROUD					
^{207}Bi	0.50	0.56	$^{+0.44}_{-0.37}$	0.001	0.003
OTHER					
^{42}K in LAr	0.2019	0.2004	± 0.0038	0.377	0.471
^{42}K on COAX n ⁺ [cts]	660	630	± 170	–	0.379
α -model BEGe [cts]	1343	1332	± 50	0.416	–
α -model COAX [cts]	2955	2962	± 78	–	0.470
TOTAL				1.38 ± 0.65	1.83 ± 0.82
p-value					
0.94					

that scale. The chosen values to estimate this contribution were 10, 15, 20, 25, 30 keV. A mean of the deviations of $T_{1/2}^{2\nu}$ from (37) has been computed to provide a rough estimate, found to be $\pm 1.2\%$, of the contribution of the binning choice to the total systematic uncertainty.

- ◊ Some contributions could arise from the reliability of the Monte Carlo simulations. The main sources can be two: the accuracy of the implementation of the GERDA geometry in MAGE, e.g. the rounding of the detector corners, and the accuracy of the particle propagation algorithms in GEANT4, which depends on the uncertainties on cross-sections and final states. The two contributions were estimated in previous works to be 1% [60] and 2% [61–63] respectively.
- ◊ The uncertainties on the active volume fraction f_{av} can enter in the model in several ways. On one hand, they affect the simulations of particle decays inside the detectors, such as $2\nu\beta\beta$, because the fraction of decays taking place in the active and in the dead part of the detector changes with f_{av} . The uncertainties on the values of f_{av} for BEGe and enriched coaxial detectors are of the order $\sim 3\%$ and $\sim 6\%$, respectively, as it can be deduced from Tab. 1 and Tab. 2. The analysis was repeated twice, by replacing the $2\nu\beta\beta$ energy spectra with those generated with the lower limit and those generated with the upper limit for f_{av} . The results on $T_{1/2}^{2\nu}$ are stable within $^{+3.9}_{-2.5}\%$.

The uncertainty on the active volume fraction could also play a role in the shape of the energy spectrum due to ^{42}K decays on the n^+ surface. However this contribution is expected to be negligible in the present analysis. An analogous computation for GERDA Phase I data, where none of the ^{42}K contaminations on p^+ and n^+ surfaces (of both BEGe and enriched coaxial detectors) were excluded by the fitting procedure, already showed this [64]. Moreover, in the present analysis, only the ^{42}K contamination on the n^+ contact of the coaxial detectors survived in the minimal model, thus the contribution to the systematic uncertainty is expected to be further suppressed.

- ◊ The uncertainties on the enrichment fraction f_{76} also affect the estimate of $T_{1/2}^{2\nu}$. Their effect was evaluated in a similar manner as for the f_{av} uncertainties. The uncertainty on f_{76} for the detectors is $\sim 1.5\%$, except for ANG1, ANG2 and ANG3, for which it is around $\sim 3\%$. Again, the analysis was repeated for the lower and upper limits of f_{76} and the result on $T_{1/2}^{2\nu}$ was found stable within $^{+2.0}_{-1.6}\%$.
- ◊ A contribution could also arise from the reliability of data acquisition and selection algorithms, but it is expected to be very small. As possible sources, the calculation of the live time as well as reconstruction and trigger efficiencies have to be considered. Also, some unphysical events could still be present in the data set. The impact of this component is expected to be not larger than 0.5% for $T_{1/2}^{2\nu}$.
- ◊ A last contribution could come from the approximations used in DECAY0 to compute the $2\nu\beta\beta$ energy spectrum. As mentioned before, this calculation is in

Table 9: Single contributions to the systematic uncertainties on $T_{1/2}^{2\nu}$ and the 90% quantile of the posterior distribution of $\dot{a}_{\text{of}}^{(3)}$.

Contribution	$T_{1/2}^{2\nu}$ [%]	$\dot{a}_{\text{of}}^{(3)}$ [%]
Binning	± 1.2	± 14.3
MC geometry		± 1.0
MC tracking		± 2.0
Active volume fraction	$+3.9$ -2.5	$+3.8$ -1.7
Enrichment fraction	$+2.0$ -1.6	$+2.0$ -1.8
Data acquisition and selection		± 0.5
Total	$+5.1$ -3.9	$+15.1$ -14.7

principle more precise than the one with the Primakoff-Rosen approximation, and has been cross-checked in other experiments. Thus this contribution is expected to be negligible in the present analysis.

The single contributions to the systematic uncertainty are listed in Tab. 9. The total systematic uncertainty on $T_{1/2}^{2\nu}$ was obtained by summing in quadrature the single contributions.

The final result on $T_{1/2}^{2\nu}$, with the statistic and systematic uncertainties, is

$$\begin{aligned} T_{1/2}^{2\nu} &= (1.984 \quad {}^{+0.020}_{-0.020\text{stat}} \quad {}^{+0.098}_{-0.075\text{sys}}) \cdot 10^{21} \text{ yr} \\ &= (1.98 \quad {}^{+0.10}_{-0.08}) \cdot 10^{21} \text{ yr}, \end{aligned} \quad (38)$$

which is compatible with the result of GERDA Phase I (35). After the inclusion of the systematic uncertainties the relative error on $T_{1/2}^{2\nu}$ increases from 1% to 5%. The total error is clearly dominated by its systematic component, in particular by the uncertainties on the active volume fraction f_{av} and on the enrichment fraction f_{76} . A campaign of accurate measurements of the properties of the detectors could further improve the present estimate.

Lorentz-violating double-beta decay mode

The minimal background model described in the previous section and the result on $T_{1/2}^{2\nu}$ were used to put an upper limit on the Lorentz-violating double-beta decay component simply adding the new spectrum shape with $\dot{a}_{\text{of}}^{(3)}$ as the fitted parameter, as described in 4, and leaving the $T_{1/2}^{2\nu}$ values fluctuate around (38) within the uncertainties.

The results are given in Tab. 10 and the marginalised posterior distribution for $\dot{a}_{\text{of}}^{(3)}$, in electron mass units, is shown in Fig. 15, black histogram. The distribution shows a

non-zero mode, but is consistent with zero at the 90% C.L. The upper limit for $\dot{a}_{\text{of}}^{(3)}$ was determined as the 90% quantile of this distribution:

$$\dot{a}_{\text{of}}^{(3)} < 7.4 \cdot 10^{-8} \text{ GeV} \quad (90\% \text{ C.L.}) \quad (39)$$

Systematic uncertainties

The systematic uncertainties on the $\dot{a}_{\text{of}}^{(3)}$ estimation were calculated following the same procedure discussed for $T_{1/2}^{2\nu}$, now looking to the stability of the 90% quantile of the $\dot{a}_{\text{of}}^{(3)}$ posterior distribution. The analysis was repeated for the same different bin sizes and then a mean was performed between the deviations from (39), also the same upper limits for f_{av} and f_{76} were considered to estimate the corresponding contributions. The same uncertainties for the Monte Carlo accuracy and data acquisition and selection were assumed. Summing in quadrature all the contributions we obtain $^{+15.1}_{-14.7}\%$ as the total systematic uncertainty on the 90% quantile. The results are summarized in Tab. 9.

To include the systematic uncertainties in the $\dot{a}_{\text{of}}^{(3)}$ upper limit the following method has been adopted. Once the total lower and upper systematic uncertainties are known, an asymmetric gaussian distribution representing the systematic uncertainty can be built. This distribution was composed by two normal distributions centered in $\mu = 1$ with right and left widths corresponding to the positive and negative part of the systematic uncertainty, respectively. In order to fold this function in the posterior probability distribution of $\dot{a}_{\text{of}}^{(3)}$, a random number r following the systematic uncertainty distribution was generated for each entry p in the posterior distribution. A new histogram was filled with the product $p \cdot r$. This new distribution represents the final posterior distribution, comprising the statistical and systematic uncertainties (see Fig. 15). The final result for $\dot{a}_{\text{of}}^{(3)}$ was determined as the 90% quantile of this distribution:

$$\dot{a}_{\text{of}}^{(3)} < 7.5 \cdot 10^{-8} \text{ GeV} \quad (90\% \text{ C.L.}) \quad (40)$$

The corresponding Lorentz-violating spectrum is reported in Fig. 16 along with the Standard Model mode.

COMMENTS

To compare our result with previous estimates two other works have been considered. In [17] an outside analysis on the endpoint of the Troitsk and Mainz tritium beta decay data has been performed, yielding a conservative upper limit for the parameter of interest of $\dot{a}_{\text{of}}^{(3)} \lesssim 1 \cdot 10^{-9} \text{ GeV}$, which is more than an order of magnitude more stringent than the one obtained in this work. This constraint improves limits extracted from threshold effects occurring in pion and kaon decays in the presence of unconventional dispersion relations for neutrinos. However, our result fully takes into account for experimental background and systematic uncertainties, and thus is much more valuable than the limits reported above.

A recent result by the EXO-200 collaboration [18], that also studies double-beta decay data, has been considered to which a comparison makes more sense. Their analysis

Table 10: Results for the minimal background model with informative priors and the Lorentz-violating $2\nu\beta\beta$ component. The global and the marginalised mode, together with the 1σ -contour of the marginalised distribution are provided. The Background Index (BI) summed separately over BEGe and enriched coaxial detectors is also given (the field is left blank when the Q-value of the background source is below the ROI). The presence of an underlying informative prior distribution is marked with (\dagger).

Source	Global [mBq/kg]	Marg. [mBq/kg]	1σ [mBq/kg]	BI [BEGe] [10^{-2} cts/(keV·kg·yr)]	BI [COAX]
$T_{1/2}^{2\nu}$ [10^{21} yr] (fixed)	1.984	–	–	0.001	0.001
FIBERS					
^{40}K	82.43	77.55	$^{+13}_{-14}$	–	–
$^{212}\text{Bi} + ^{208}\text{Tl}$ (\dagger)	0.0556	0.0591	± 0.012	0.002	0.002
$^{214}\text{Pb} + ^{214}\text{Bi}$	1.81	1.64	$^{+0.68}_{-0.75}$	0.150	0.171
HOLDERS					
^{40}K (\dagger)	4.64	4.13	0.86	–	–
$^{214}\text{Pb} + ^{214}\text{Bi}$	0.074	0.084	$^{+0.064}_{-0.057}$	0.077	0.055
^{228}Ac	0.269	0.284	$^{+0.073}_{-0.071}$	0.005	0.004
^{60}Co	0.091	0.092	± 0.025	0.047	0.038
CABLES					
^{40}K	92	162	$^{+95}_{-85}$	–	–
$^{212}\text{Bi} + ^{208}\text{Tl}$	12.2	12.2	± 1.6	0.284	0.225
$^{234\text{m}}\text{Pa}$	4.7	3.8	$^{+3.7}_{-2.9}$	0.001	0.002
MINI-SHROUD					
^{207}Bi	0.40	0.44	$^{+0.42}_{-0.34}$	0.001	0.002
OTHER					
^{42}K in LAr	0.1973	0.1970	± 0.0037	0.374	0.467
^{42}K on COAX n ⁺ [cts]	581	635	± 170	–	0.333
α -model BEGe [cts]	1343	1330	± 50	0.415	–
α -model COAX [cts]	2947	2980	± 78	–	0.473
TOTAL				1.36 ± 0.65	1.77 ± 0.81
p-value					0.95

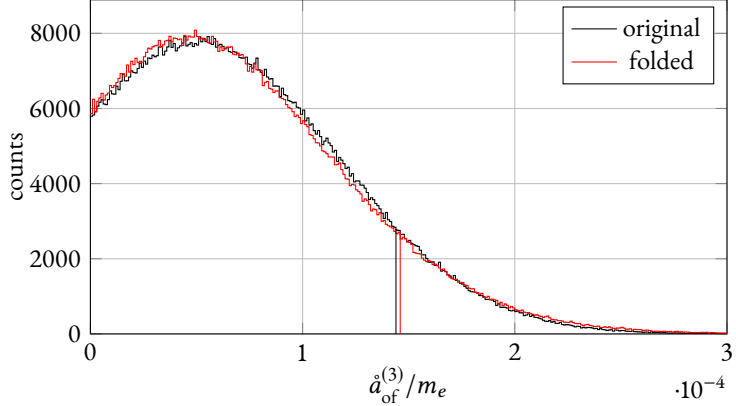


Figure 15: Posterior distribution of $\hat{a}_{\text{of}}^{(3)}$ (in units of electron mass) before and after folding with the systematic uncertainty distribution.

reported a result which is $\hat{a}_{\text{of}}^{(3)} < 7.6 \cdot 10^{-6}$ GeV at 90% C.L., two orders of magnitude higher than our result. This improvement can be attributed to the superior energy resolution achievable with the GERDA detector array, that allows to better constrain the contributions in the background model.

Conclusions

In this work, a first search for Lorentz-violating effects governed by the $\hat{a}_{\text{of}}^{(3)}$ isotropic coefficient using double-beta decay data from GERDA Phase II has been performed. A Bayesian statistical analysis was employed to operate a background decomposition separately on the BEGe and enriched coaxial data sets, using, where available, radioactivity measures from material screening to constraint the fit or cross-checking the results. A large contribution from ${}^{40}\text{K}$ in far locations of the experimental apparatus is found, not indicated by material screening. The final result for the Standard Model two-neutrino double-beta decay half-life $T_{1/2}^{2\nu}$, with the statistical and systematic uncertainties, is:

$$T_{1/2}^{2\nu} = (1.984 \begin{array}{l} +0.020 \\ -0.020 \text{stat} \end{array} \begin{array}{l} +0.098 \\ -0.075 \text{sys} \end{array}) \cdot 10^{21} \text{ yr} \\ = (1.98 \begin{array}{l} +0.10 \\ -0.08 \end{array}) \cdot 10^{21} \text{ yr.} \quad (41)$$

With the present background model an upper limit for the $\hat{a}_{\text{of}}^{(3)}$ parameter, comprising the systematic uncertainties, was computed:

$$\hat{a}_{\text{of}}^{(3)} < 7.5 \cdot 10^{-8} \text{ GeV} \quad (90\% \text{ C.L.}) \quad (42)$$

and compared with similar analysis in the literature. Our result is found to be two orders of magnitude better than the one obtained with the EXO-200 double-beta decay data [18].

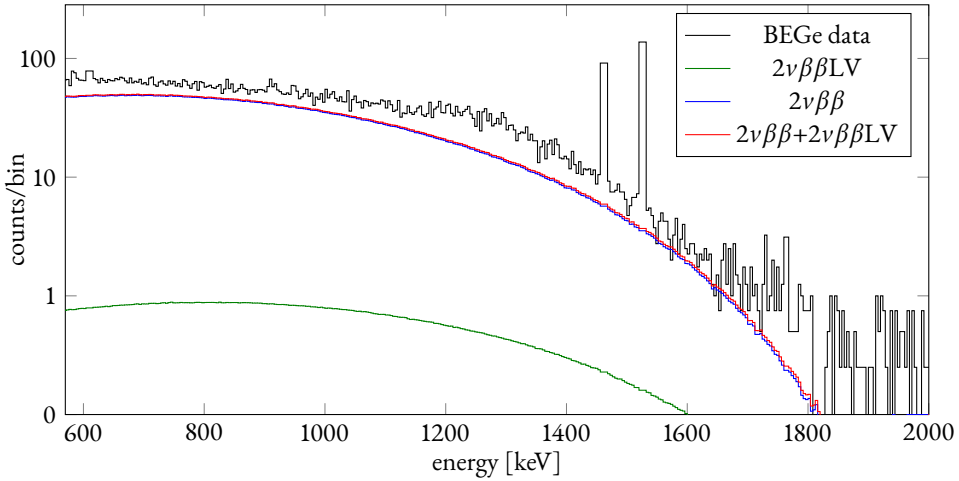


Figure 16: Double beta fitted spectra for the BEGe data set: the black histogram represents the data, the blue shape is the Standard Model double-beta decay mode, the green one is the Lorentz-violating mode with $\dot{a}_\text{of}^{(3)}$ at 90% C.I. and the red one is the sum between the two modes.

Acknowledgements

We would like to thank Ann-Kathrin Schütz for all valuable help and discussions in building up the background model and Andreas Zschocke for providing some of the simulations. We also would like to thank Rizalina Mingazheva for providing the calibrations curves.

This thesis work has been written in \LaTeX with the ‘EB Garamond’ package, a revival of Claude Garamont’s famous humanist typeface from the mid-16th century, by Georg Duffner⁶

⁶EB Garamond is free software under the terms of the SIL Open Fonts License (ofl). Development is currently done at <https://github.com/georgd/EB-Garamond>.

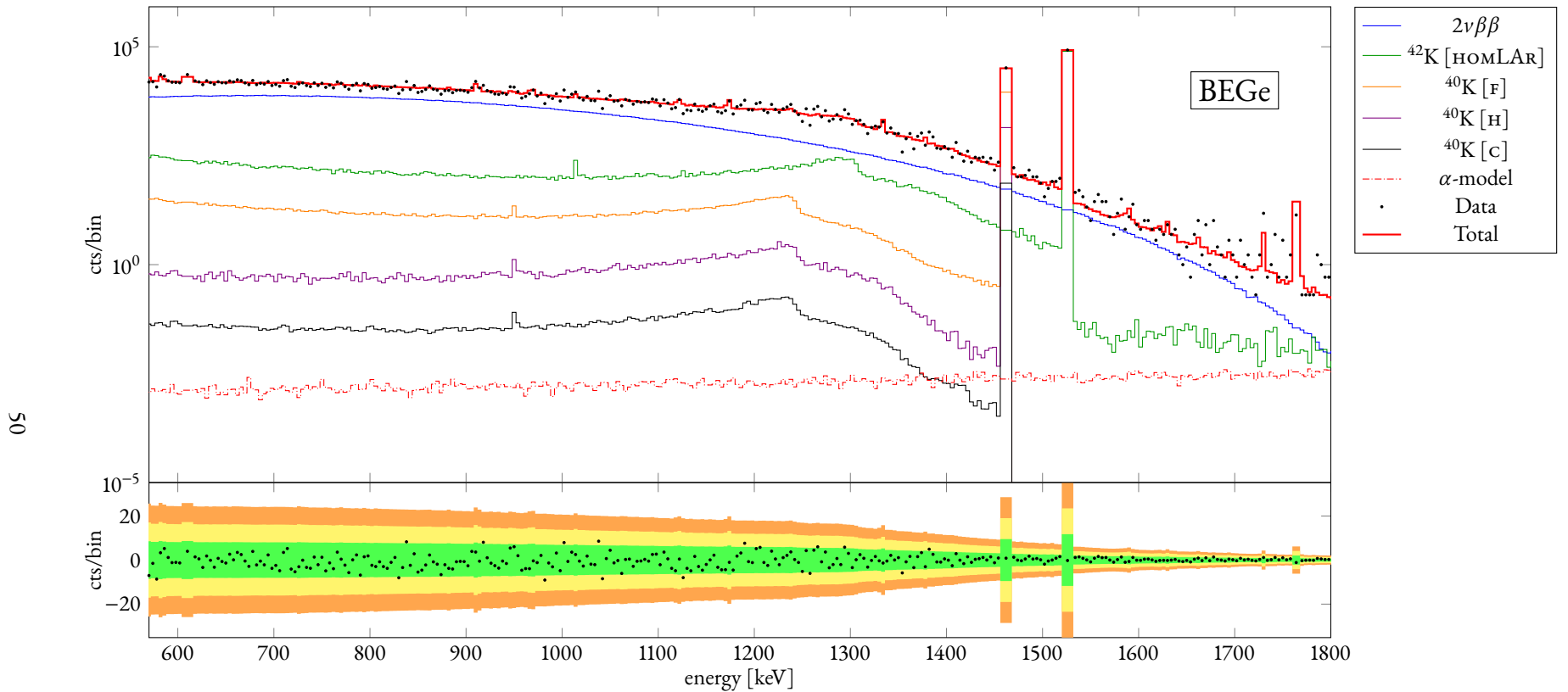


Figure 17: Part of the background decomposition in the range [570, 1800] keV for the summed BEGe energy spectrum resulting from the minimal model with informative priors. The ratio between the counts and the bin width is plotted against the energy. The residuals, computed as the subtraction between the data and the total fitted curve, is also shown. Legend: [HOMLAr] = homogeneous in LAr, [F] = fiber-shroud, [H] = holder mounting, [MS] = mini-shroud, [C] = cables, [n^+] = n^+ -contact.

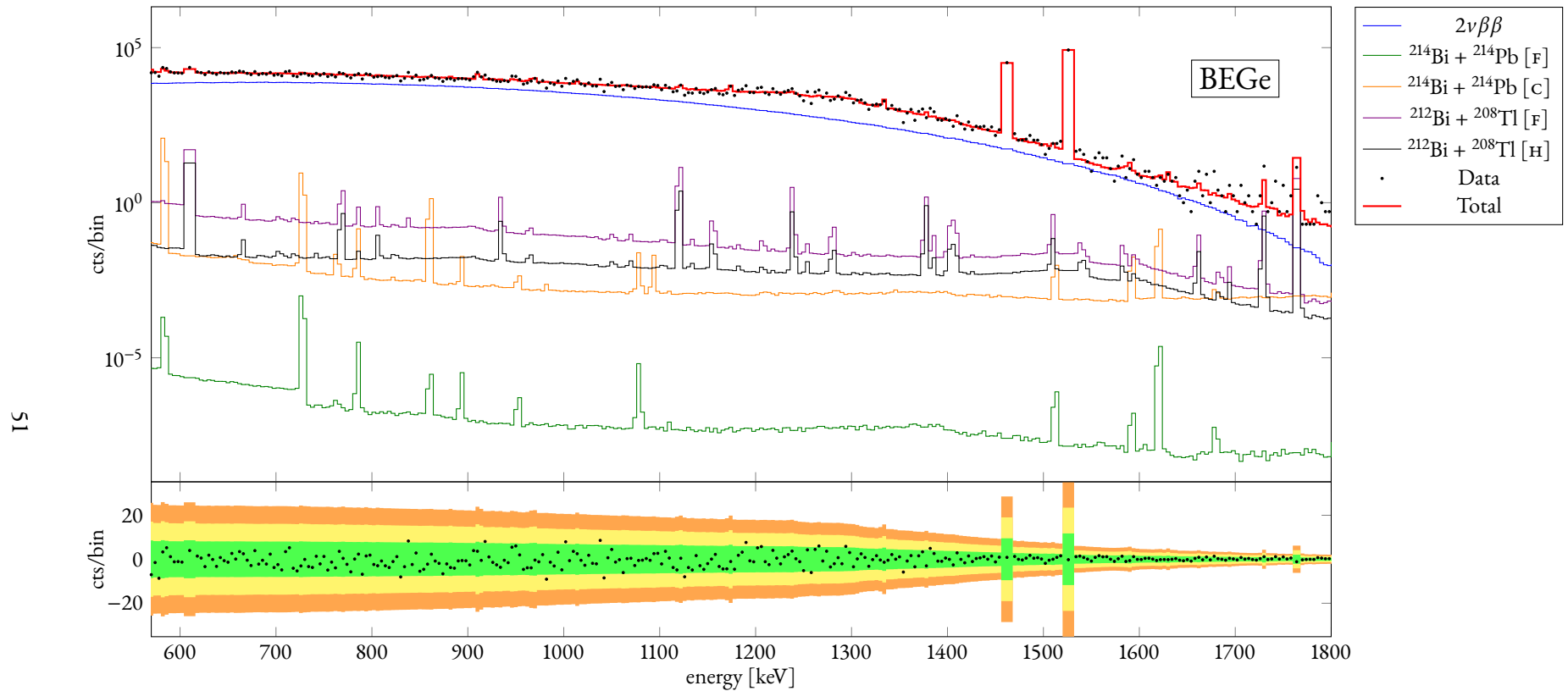


Figure 18: Part of the background decomposition in the range [570, 1800] keV for the summed BEGe energy spectrum resulting from the minimal model with informative priors. The ratio between the counts and the bin width is plotted against the energy. The residuals, computed as the subtraction between the data and the total fitted curve, is also shown. Legend: [HOMLAr] = homogeneous in LAr, [F] = fiber-shroud, [H] = holder mounting, [MS] = mini-shroud, [C] = cables, [n^+] = n^+ -contact.

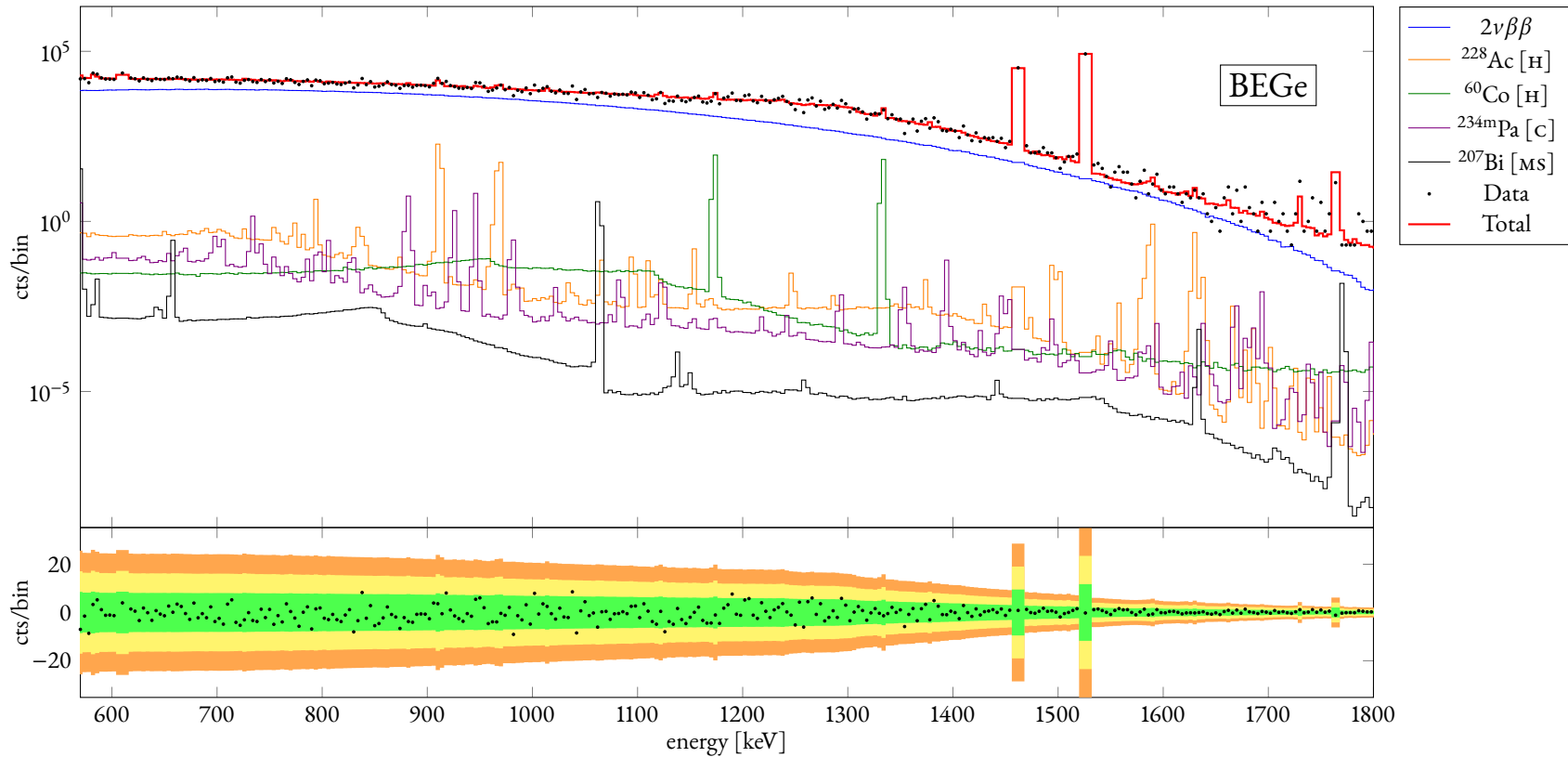


Figure 19: Part of the background decomposition in the range [570, 1800] keV for the summed BEGe energy spectrum resulting from the minimal model with informative priors. The ratio between the counts and the bin width is plotted against the energy. The residuals, computed as the subtraction between the data and the total fitted curve, is also shown. Legend: [HOMLAr] = homogeneous in LAr, [F] = fiber-shroud, [H] = holder mounting, [MS] = mini-shroud, [C] = cables, [n^+] = n^+ -contact.

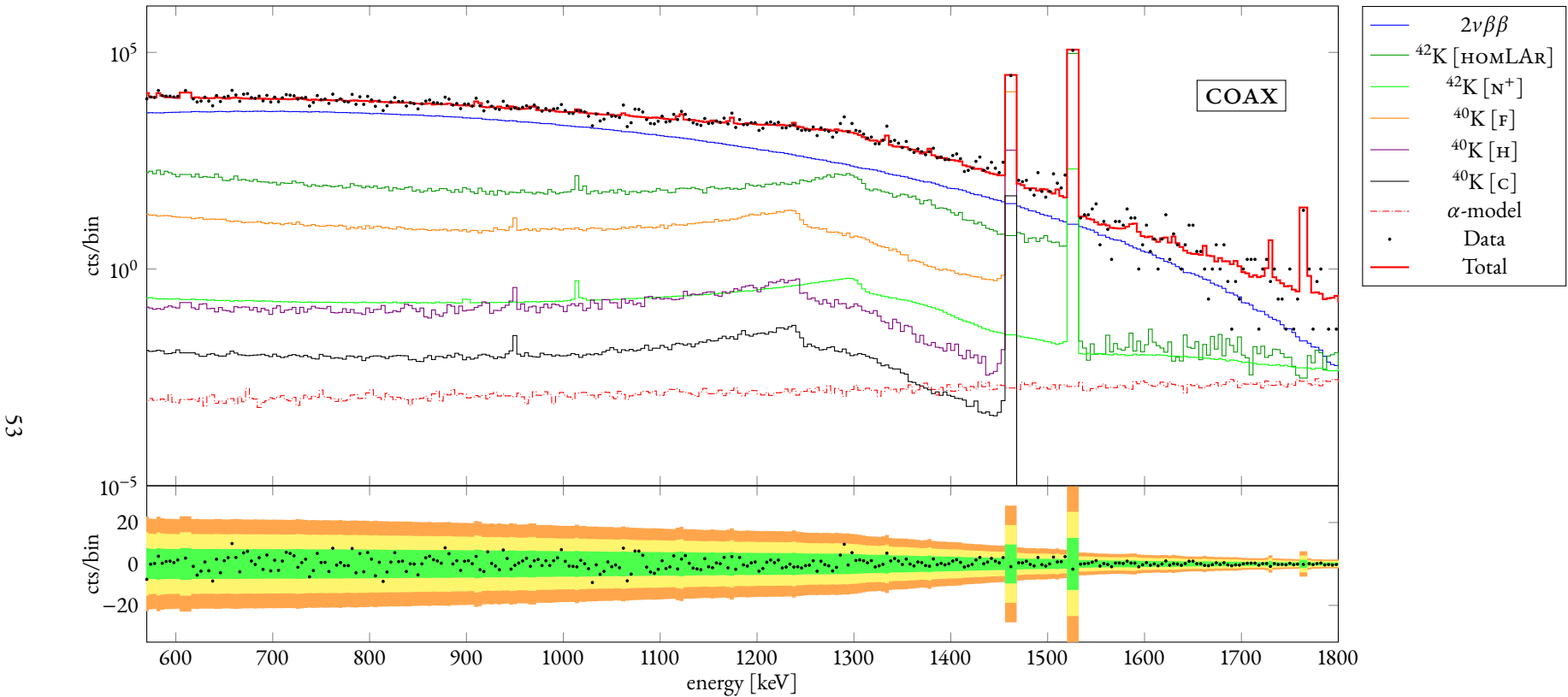


Figure 20: Part of the background decomposition in the range [570, 1800] keV for the summed enriched coaxial energy spectrum resulting from the minimal model with informative priors. The ratio between the counts and the bin width is plotted against the energy. The residuals, computed as the subtraction between the data and the total fitted curve, is also shown. Legend: [HOMLAR] = homogeneous in LAr, [F] = fiber-shroud, [H] = holder mounting, [MS] = mini-shroud, [C] = cables, [N^+] = n^+ -contact.

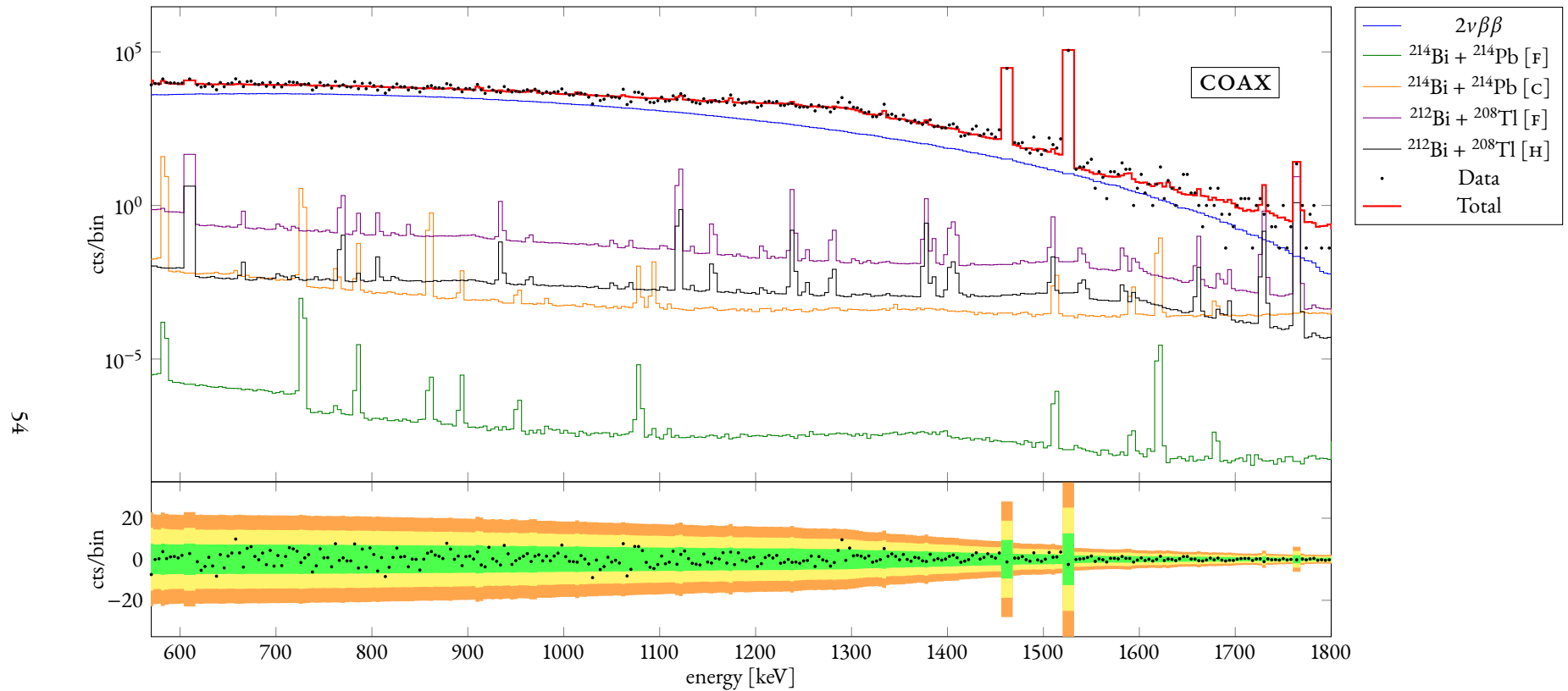


Figure 21: Part of the background decomposition in the range [570, 1800] keV for the summed enriched coaxial energy spectrum resulting from the minimal model with informative priors. The ratio between the counts and the bin width is plotted against the energy. The residuals, computed as the subtraction between the data and the total fitted curve, is also shown. Legend: [HOMLAr] = homogeneous in LAr, [F] = fiber-shroud, [H] = holder mounting, [MS] = mini-shroud, [C] = cables, [n^+] = n^+ -contact.

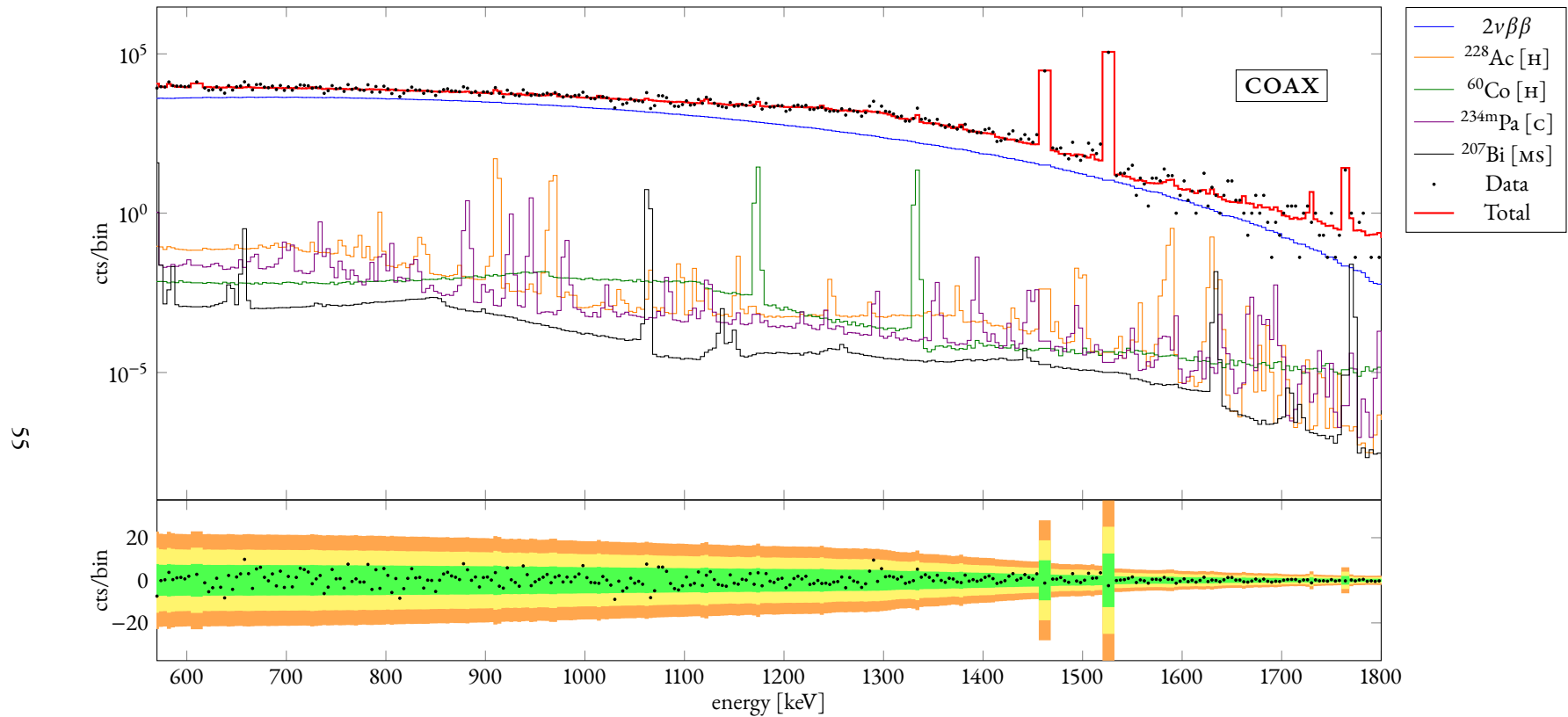


Figure 22: Part of the background decomposition in the range [570, 1800] keV for the summed enriched coaxial energy spectrum resulting from the minimal model with informative priors. The ratio between the counts and the bin width is plotted against the energy. The residuals, computed as the subtraction between the data and the total fitted curve, is also shown. Legend: [HOMLAr] = homogeneous in LAr, [F] = fiber-shroud, [H] = holder mounting, [MS] = mini-shroud, [C] = cables, [n^+] = n^+ -contact.

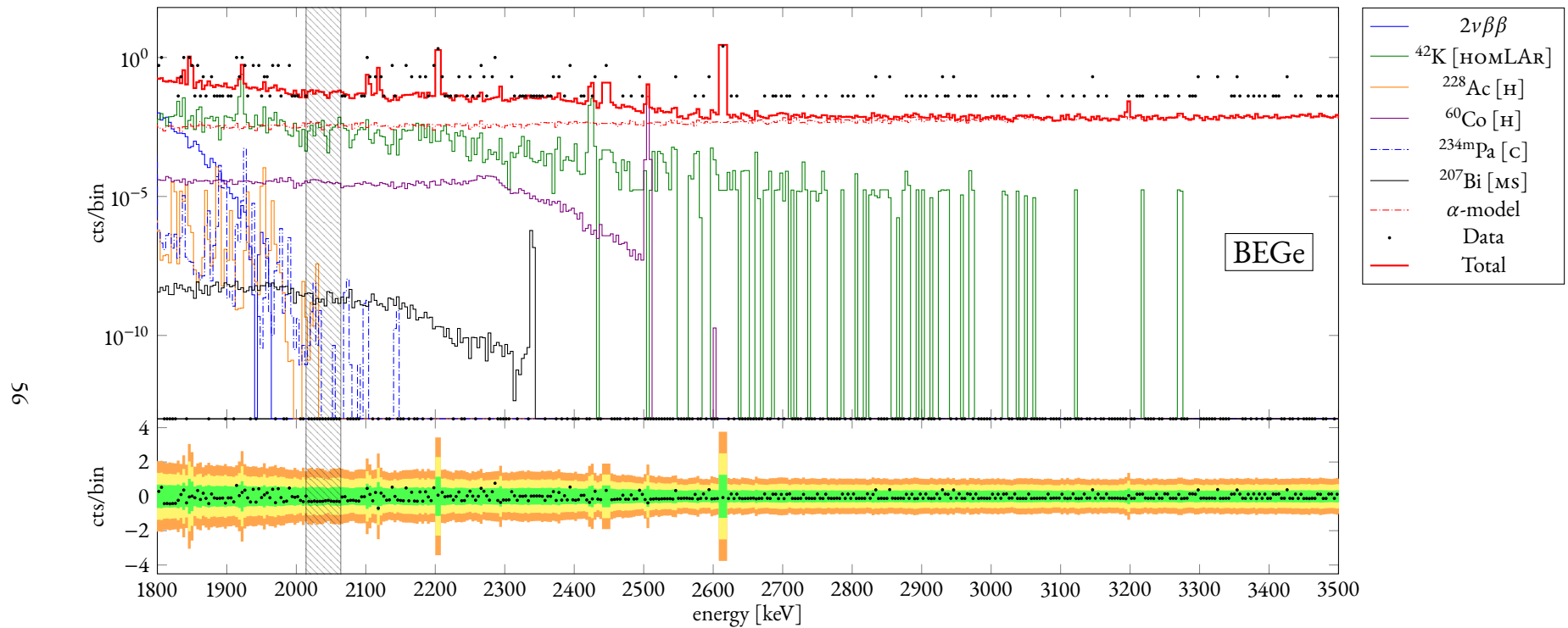


Figure 23: Part of the background decomposition in the range [1800, 3500] keV for the summed BEGe energy spectrum resulting from the minimal model with informative priors. The ratio between the counts and the bin width is plotted against the energy. The residuals, computed as the subtraction between the data and the total fitted curve, is also shown. Legend: [HOMLAR] = homogeneous in LAr, [F] = fiber-shroud, [H] = holder mounting, [MS] = mini-shroud, [C] = cables, [N^+] = n^+ – contact.

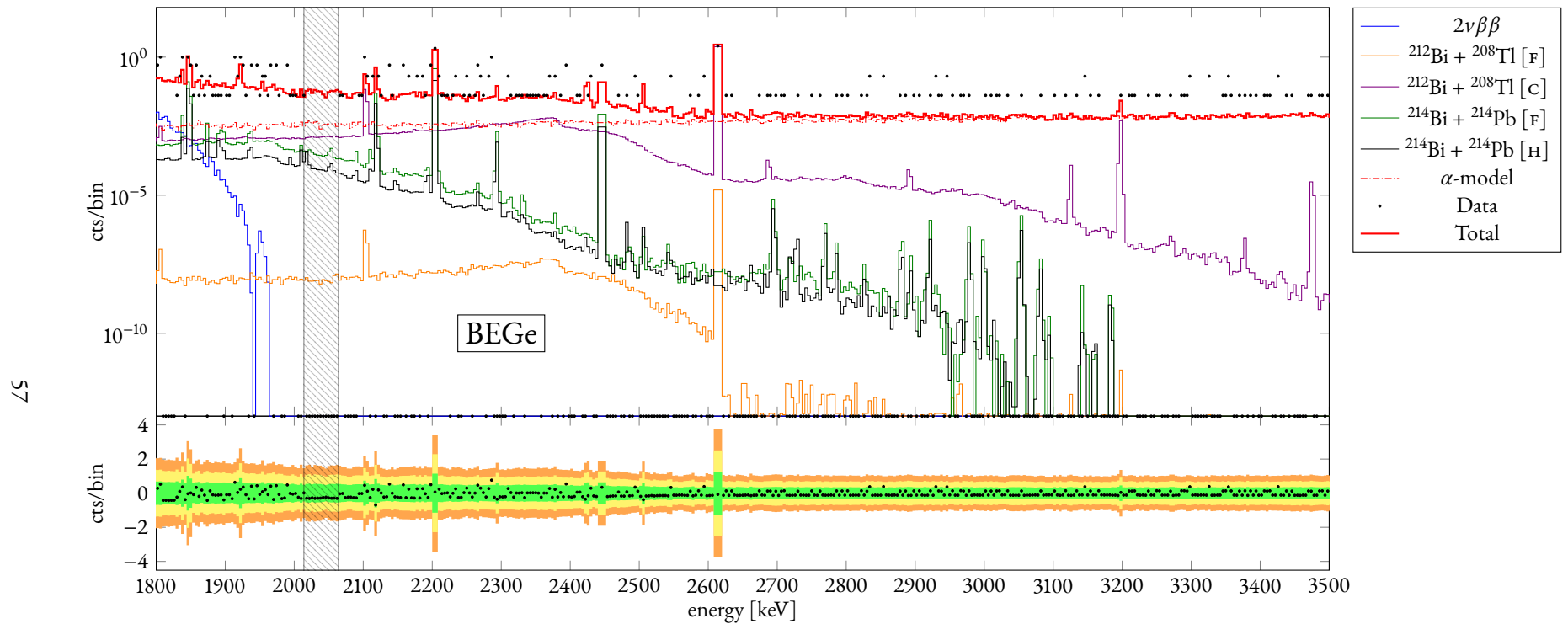


Figure 24: Part of the background decomposition in the range [1800, 3500] keV for the summed BEGe energy spectrum resulting from the minimal model with informative priors. The ratio between the counts and the bin width is plotted against the energy. The residuals, computed as the subtraction between the data and the total fitted curve, is also shown. Legend: [HOMLAr] = homogeneous in LAr, [F] = fiber-shroud, [H] = holder mounting, [MS] = mini-shroud, [C] = cables, [N^+] = n^+ -contact.

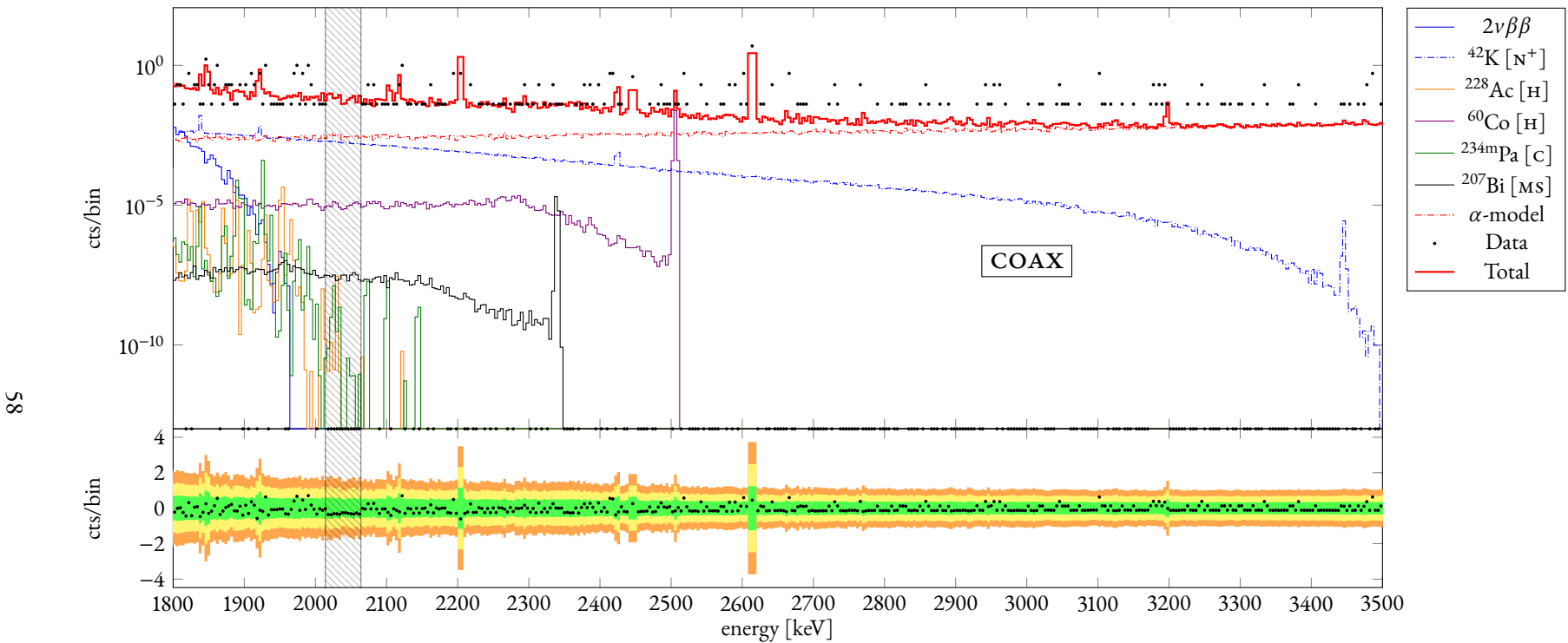


Figure 25: Part of the background decomposition in the range [1800, 3500] keV for the summed enriched coaxial energy spectrum resulting from the minimal model with informative priors. The ratio between the counts and the bin width is plotted against the energy. The residuals, computed as the subtraction between the data and the total fitted curve, is also shown. Legend: [HOMLAr] = homogeneous in LAr, [F] = fiber-shroud, [H] = holder mounting, [MS] = mini-shroud, [C] = cables, [N^+] = n^+ -contact.

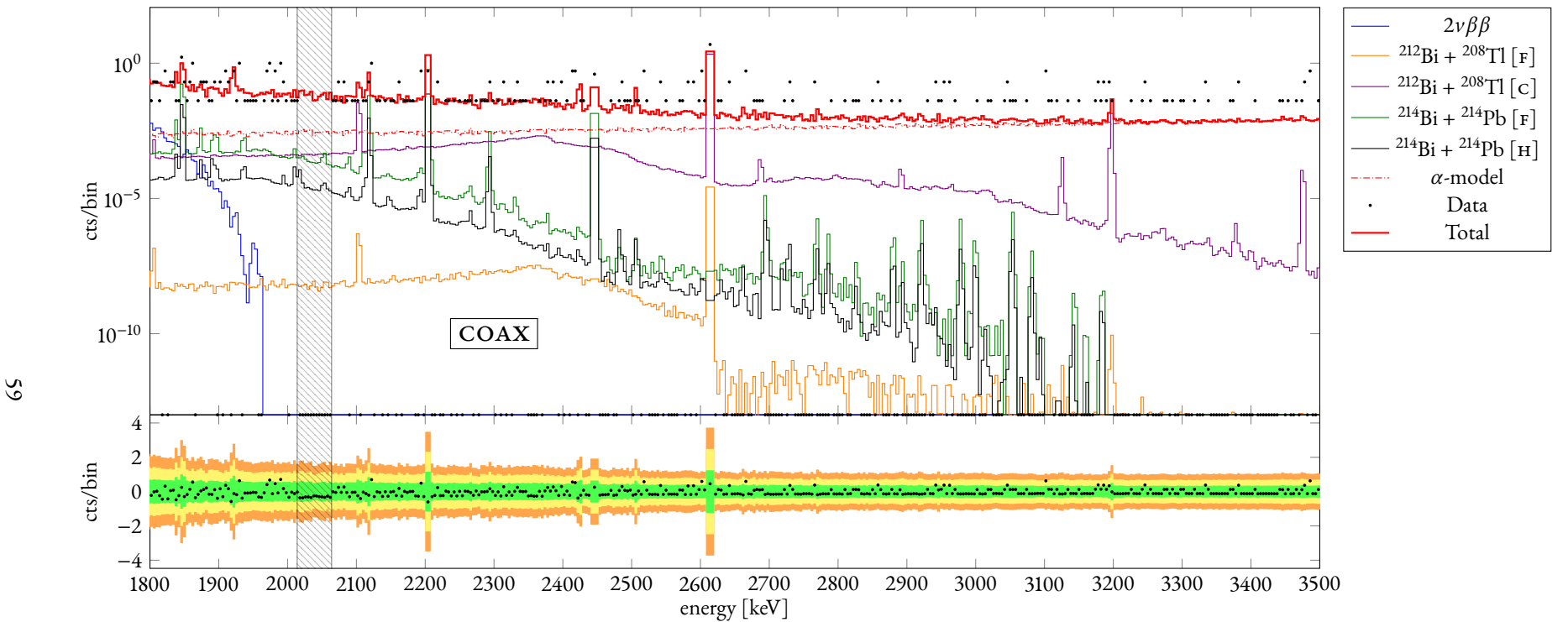


Figure 26: Part of the background decomposition in the range [1800, 3500] keV for the summed enriched coaxial energy spectrum resulting from the minimal model with informative priors. The ratio between the counts and the bin width is plotted against the energy. The residuals, computed as the subtraction between the data and the total fitted curve, is also shown. Legend: [HOMLAr] = homogeneous in LAr, [F] = fiber-shroud, [H] = holder mounting, [MS] = mini-shroud, [C] = cables, [n^+] = n^+ -contact.

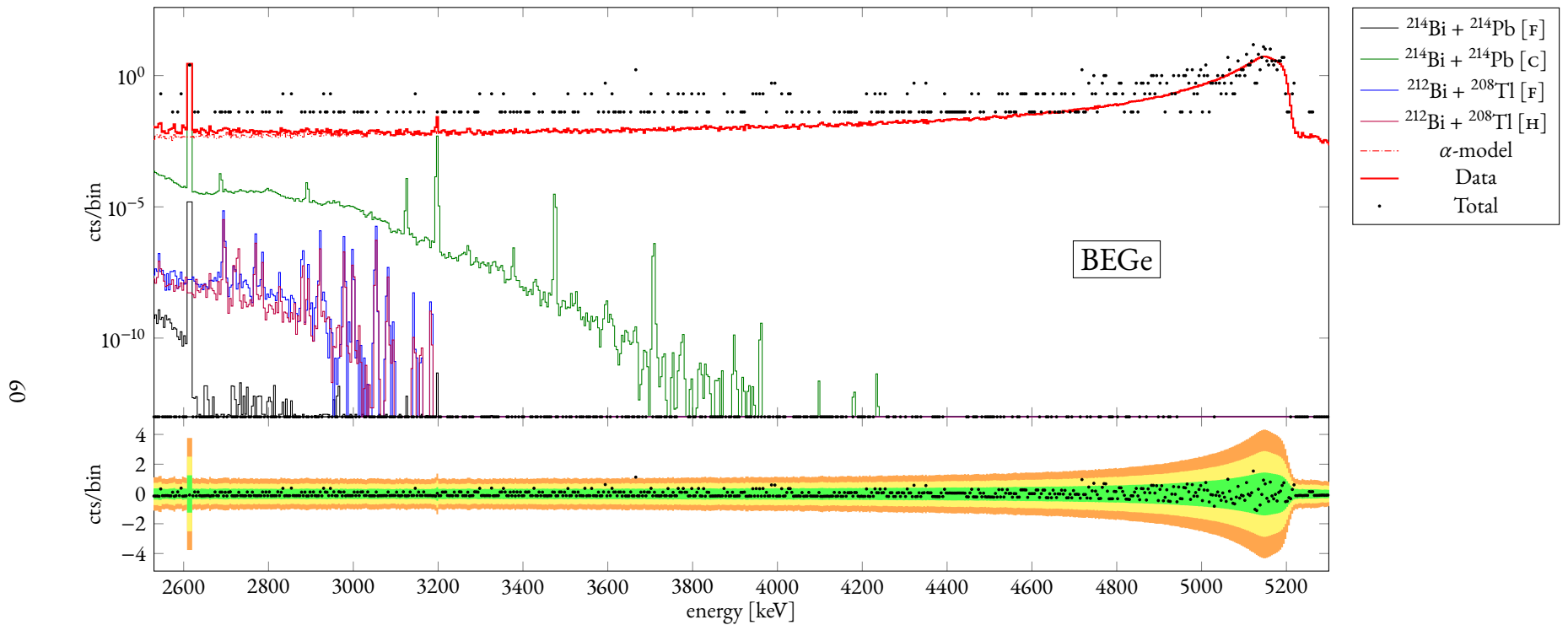


Figure 27: Part of the background decomposition in the range [2500, 5300] keV for the summed BEGe energy spectrum resulting from the minimal model with informative priors. The ratio between the counts and the bin width is plotted against the energy. The residuals, computed as the subtraction between the data and the total fitted curve, is also shown. Legend: [HOMLAr] = homogeneous in LAr, [F] = fiber-shroud, [H] = holder mounting, [MS] = mini-shroud, [C] = cables, [N^+] = n^+ -contact.

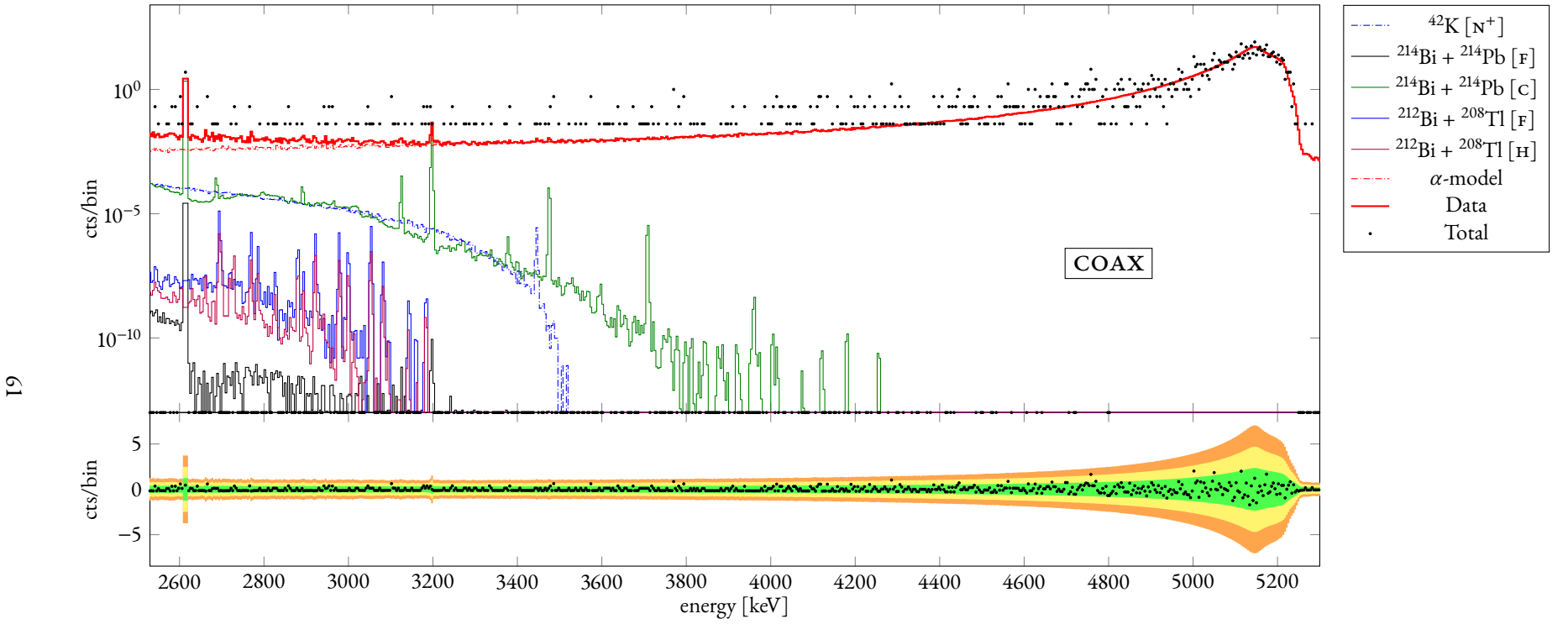


Figure 28: Part of the background decomposition in the range [2500, 5300] keV for the summed enriched coaxial energy spectrum resulting from the minimal model with informative priors. The ratio between the counts and the bin width is plotted against the energy. The residuals, computed as the subtraction between the data and the total fitted curve, is also shown. Legend: [HOMLAr] = homogeneous in LAr, [F] = fiber-shroud, [H] = holder mounting, [MS] = mini-shroud, [C] = cables, [N^+] = n^+ -contact.

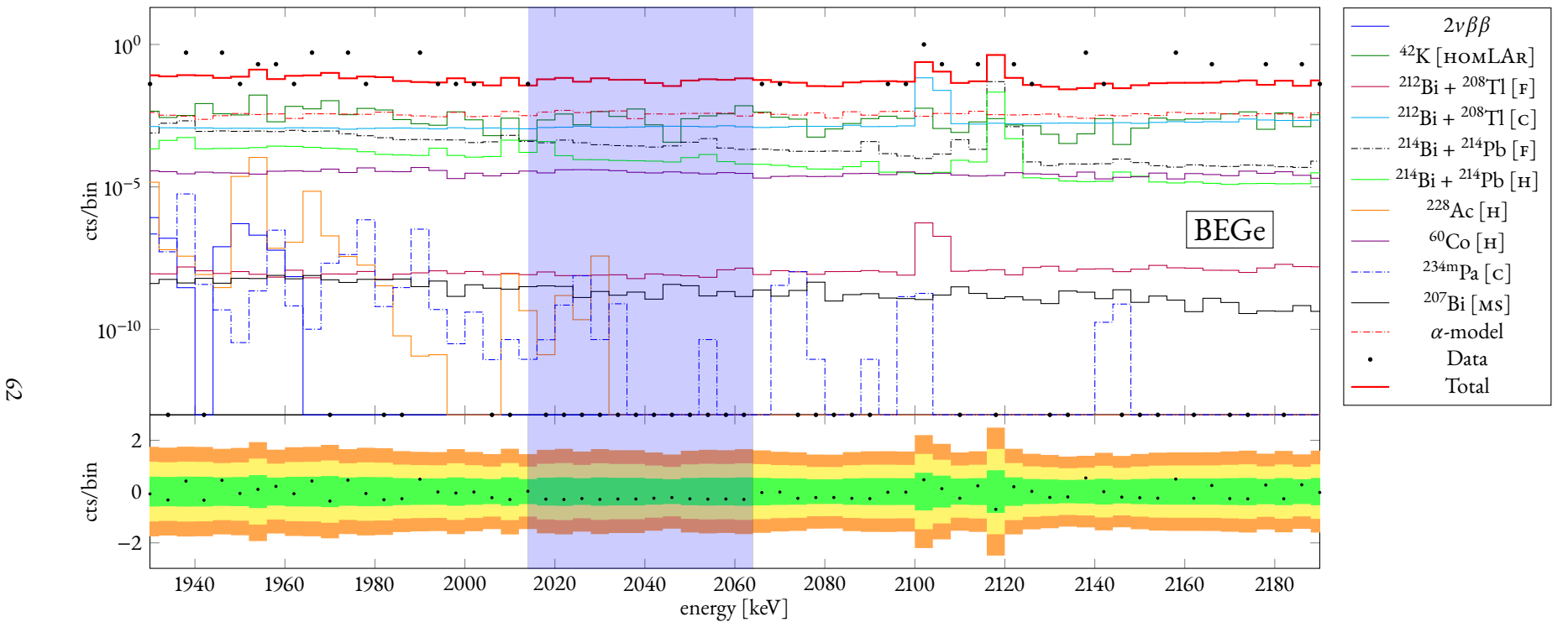


Figure 29: Background decomposition in the range [1930, 2190] keV (the ROI) for the summed BEGe energy spectrum resulting from the minimal model with informative priors. The ratio between the counts and the bin width is plotted against the energy. The residuals, computed as the subtraction between the data and the total fitted curve, is also shown. Legend: [HOMLAR] = homogeneous in LAr, [F] = fiber-shroud, [H] = holder mounting, [MS] = mini-shroud, [C] = cables, [N^+] = n^+ -contact.

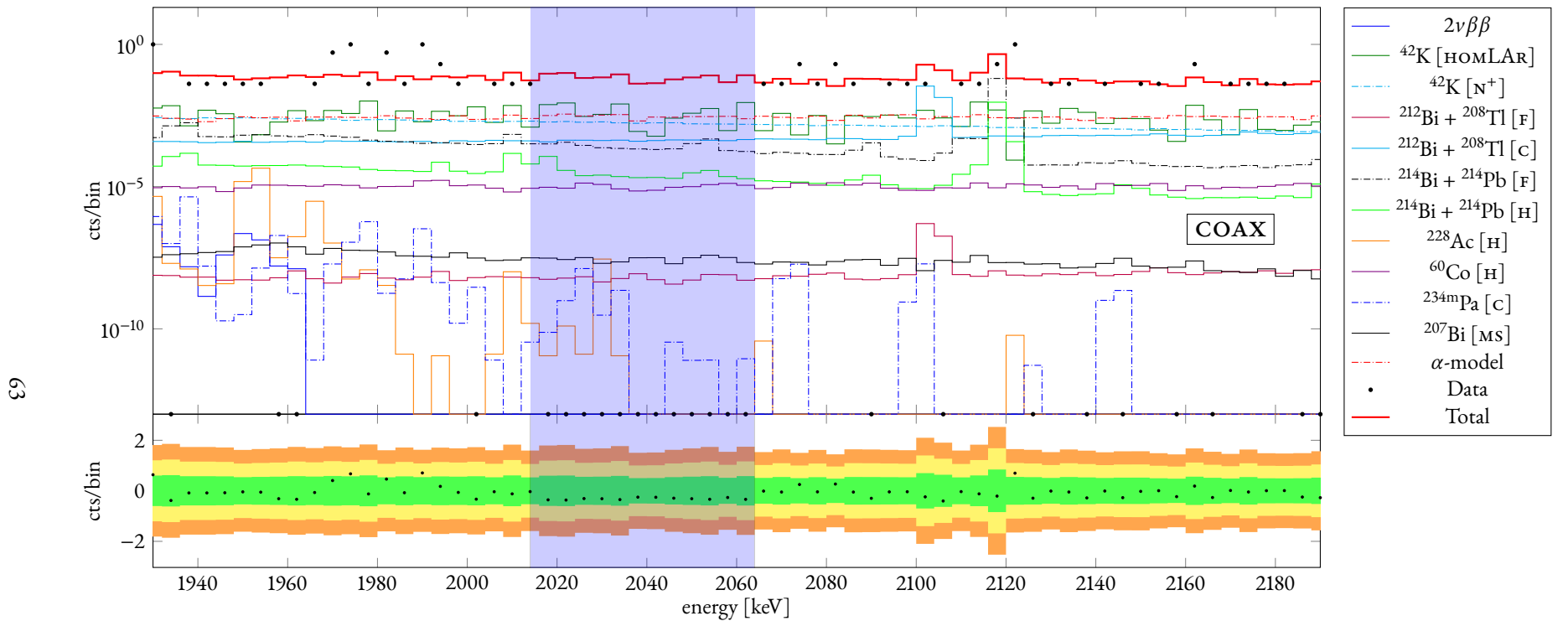


Figure 30: Background decomposition in the range [1930, 2190] keV (the RoI) for the summed enriched coaxial energy spectrum resulting from the minimal model with informative priors. The ratio between the counts and the bin width is plotted against the energy. The residuals, computed as the subtraction between the data and the total fitted curve, is also shown. Legend: [HOMLAr] = homogeneous in LAr, [F] = fiber-shroud, [H] = holder mounting, [MS] = mini-shroud, [C] = cables, [N^+] = n^+ -contact.

References

1. GOEPPERT-MAYER M. *Phys. Rev.* 48:512, 1935. doi:10.1103/PhysRev.48.512
2. GIUNTI C. et al. Fundamentals of Neutrino Physics and Astrophysics. Oxford University Press, 2007
3. TOMODA T. *Rep. Prog. Phys.* 54(1):53, 1991
4. HAXTON W.C. et al. *Prog. Part. Nucl. Phys.* 12:409, 1984. doi:10.1016/0146-6410(84)90006-1
5. DOI M. et al. *Prog. Theor. Phys.* 66(5):1739, 1981. doi:10.1143/PTP.66.1739
6. DOI M. et al. *Prog. Theor. Phys.* 69(2):602, 1983. doi:10.1143/PTP.69.602
7. PRIMAKOFF H. et al. *Rep. Prog. Phys.* 22(1):121, 1959. doi:10.1088/0034-4885/22/1/305
8. FURRY W.H. *Phys. Rev.* 56:1184, 1939. doi:10.1103/PhysRev.56.1184
9. MAJORANA E. *Il Nuovo Cimento* 9(10):335, 1932. doi:10.1007/BF02959557
10. RODEJOHANN W. *Int. J. Mod. Phys.* E20:1833, 2011. doi:10.1142/S0218301311020186
11. COLLADAY D. et al. *Phys. Rev. D* 55:6760, 1997. doi:10.1103/PhysRevD.55.6760
12. COLLADAY D. et al. *Phys. Rev. D* 58:116002, 1998. doi:10.1103/PhysRevD.58.116002
13. KOSTELECKÝ V.A. et al. *Phys. Rev. D* 85:096005, 2012. doi:10.1103/PhysRevD.85.096005
14. KOSTELECKÝ V.A. et al. *Phys. Rev. Lett.* 102:010402, 2009. doi:10.1103/PhysRevLett.102.010402
15. BLUHM R. et al. *Phys. Rev. D* 68:125008, 2003. doi:10.1103/PhysRevD.68.125008
16. KOSTELECKÝ V.A. et al. *Phys. Rev. D* 66:056005, 2002. doi:10.1103/PhysRevD.66.056005
17. DÍAZ J.S. et al. *Phys. Rev. D* 88(7):071902, 2013. doi:10.1103/PhysRevD.88.071902
18. ALBERT J.B. et al. *Phys. Rev. D* 93:072001, 2016. doi:10.1103/PhysRevD.93.072001
19. ACKERMANN K.H. et al. *Eur. Phys. J.* C73(3):2330, 2013. doi:10.1140/epjc/s10052-013-2330-0
20. KLAUDOR-KLEINGROTHAUS H.V. et al. *Phys. Lett.* B586:198, 2004. doi:10.1016/j.physletb.2004.02.025
21. AGOSTINI M. et al. *Phys. Rev. Lett.* 111(12):122503, 2013. doi:10.1103/PhysRevLett.111.122503
22. AGOSTINI M. et al. *Nature* 544:47, 2017. doi:10.1038/nature21717
23. KLAUDOR-KLEINGROTHAUS H.V. et al. *Eur. Phys. J.* A12:147, 2001. doi:10.1007/s100500170022
24. AALSETH C.E. et al. *Phys. Rev. D* 65:092007, 2002. doi:10.1103/PhysRevD.65.092007

25. HELLMIG J. et al. *Z. Phys. A*359:351, 1997. doi:10.1007/s002180050414
26. KLAUDOR-KLEINGROTHAUS H.V. et al. *Nucl. Instrum. Meth.* A481:149, 2002. doi:10.1016/S0168-9002(01)01258-X
27. HE Z. *Nucl. Instrum. Meth.* 463(1-2):250 , 2001. doi:10.1016/S0168-9002(01)00223-6
28. BUDJÁŠ D. et al. *J. Instrum.* 4(10):P10007, 2009. doi:10.1088/1748-0221/4/10/P10007
29. BUDJÁŠ D. et al. *J. Instrum.* 8(04):P04018, 2013. doi:10.1088/1748-0221/8/04/P04018
30. AGOSTINI M. et al. *J. Instrum.* 6(03):P03005, 2011. doi:10.1088/1748-0221/6/03/P03005
31. AGOSTINI M. et al. *Eur. Phys. J. C*75(2):39, 2015. doi:10.1140/epjc/s10052-014-3253-0
32. AGOSTINI M. et al. *Eur. Phys. J. C*73(10):2583, 2013. doi:10.1140/epjc/s10052-013-2583-7
33. GRABMAYR P. et al. Re-evaluation of enrichment fractions f_{Ge} and active volume fractions f_{av} . Technical Report GSTR-13-009, 2013
34. ANDREOTTI E. et al. Full Charge Collection Depth and Active Volume of GERDA Phase II BEGe detectors. Technical Report GSTR-16-002, 2016
35. AGOSTINI M. et al. *J. Phys. Conf. Ser.* 375:042027, 2012. doi:10.1088/1742-6596/375/1/042027
36. ABGRALL N. et al. *Adv. High Energy Phys.* 2014:18, 2014. doi:10.1155/2014/365432
37. BRUN R. et al. *Nucl. Instrum. Meth.* A389:81, 1997. doi:10.1016/S0168-9002(97)00048-X
38. AGOSTINI M. et al. *J. Instrum.* 6:P08013, 2011. doi:10.1088/1748-0221/6/08/P08013
39. AGOSTINI M. et al. *J. Phys. Conf. Ser.* 368(1):012047, 2012. doi:10.1088/1742-6596/368/1/012047
40. BOSWELL M. et al. *IEEE Trans. Nucl. Sci.* 58(3 PART 3):1212, 2011. doi:10.1109/TNS.2011.2144619
41. AGOSTINELLI S. et al. *Nucl. Instrum. Meth.* A506:250, 2003. doi:10.1016/S0168-9002(03)01368-8
42. TRETYAK V. et al. *At. Data Nucl. Data Tables* 61(1):43 , 1995. doi:10.1016/S0092-640X(95)90011-X
43. PONKRATENKO O.A. et al. *Phys. Atom. Nucl.* 63:1282, 2000. doi:10.1134/1.855784. [Yad. Fiz.63,1355(2000)]
44. ARNOLD R. et al. *Nucl. Phys. A* 636(2):209 , 1998. doi:[http://dx.doi.org/10.1016/S0375-9474\(98\)00208-5](http://dx.doi.org/10.1016/S0375-9474(98)00208-5)
45. ARNOLD R. et al. *Nucl. Phys. A* 658(4):299 , 1999. doi:[http://dx.doi.org/10.1016/S0375-9474\(99\)00374-7](http://dx.doi.org/10.1016/S0375-9474(99)00374-7)
46. ARNOLD R. et al. *Nucl. Phys. A* 678(3):341 , 2000. doi:[http://dx.doi.org/10.1016/S0375-9474\(00\)00326-2](http://dx.doi.org/10.1016/S0375-9474(00)00326-2)

47. ARNOLD, R. AND OTHERS. *Nucl. Phys. A* 765(3):483 , 2006. doi:<http://dx.doi.org/10.1016/j.nuclphysa.2005.11.015>
48. ARGYRIADES J. et al. *Phys. Rev. C* 80:032501, 2009. doi:[10.1103/PhysRevC.80.032501](https://doi.org/10.1103/PhysRevC.80.032501)
49. MEIERHOFER G. et al. *Eur. Phys. J. A* 48:20, 2012. doi:[10.1140/epja/i2012-12020-y](https://doi.org/10.1140/epja/i2012-12020-y)
50. PANDOLA L. et al. *Nucl. Instrum. Meth. A* 570:149, 2007. doi:[10.1016/j.nima.2006.10.103](https://doi.org/10.1016/j.nima.2006.10.103)
51. BARABANOV I. et al. *Nucl. Instrum. Meth.* 606(3):790 , 2009. doi:[10.1016/j.nima.2009.04.006](https://doi.org/10.1016/j.nima.2009.04.006)
52. AGOSTINI G.D. Bayesian Reasoning in Data Analysis: A Critical Introduction. World Scientific Publishing Company, 2003
53. BEAUJEAN F. et al. *Phys. Rev. D* 83:012004, 2011. doi:[10.1103/PhysRevD.83.012004](https://doi.org/10.1103/PhysRevD.83.012004)
54. CALDWELL A. et al. *Comp. Phys. Comm.* 180(11):2197 , 2009. doi:[10.1016/j.cpc.2009.06.026](https://doi.org/10.1016/j.cpc.2009.06.026)
55. METROPOLIS N. et al. *J. Chem. Phys.* 21(6):1087, 1953. doi:[10.1063/1.1699114](https://doi.org/10.1063/1.1699114)
56. HASTINGS W.K. *Biometrika* 57:97, 1970. doi:[10.1093/biomet/57.1.97](https://doi.org/10.1093/biomet/57.1.97)
57. JAMES F. et al. *Comput. Phys. Commun.* 10:343, 1975. doi:[10.1016/0010-4655\(75\)90039-9](https://doi.org/10.1016/0010-4655(75)90039-9)
58. HAHN T. *Comput. Phys. Commun.* 168:78, 2005. doi:[10.1016/j.cpc.2005.01.010](https://doi.org/10.1016/j.cpc.2005.01.010)
59. DAGUM L. et al. *Comput. Sci. Eng., IEEE* 5(1):46, 1998. doi:[10.1109/99.660313](https://doi.org/10.1109/99.660313)
60. AGOSTINI M. et al. *Eur. Phys. J. C* 75(9):416, 2015. doi:[10.1140/epjc/s10052-015-3627-y](https://doi.org/10.1140/epjc/s10052-015-3627-y)
61. AMAKO K. et al. *IEEE Trans. Nucl. Sci.* 52(4):910, 2005. doi:[10.1109/TNS.2005.852691](https://doi.org/10.1109/TNS.2005.852691)
62. POON E. et al. *Med. Phys.* 32(6Part1):1696, 2005. doi:[10.1118/1.1895796](https://doi.org/10.1118/1.1895796)
63. CIRRONE G. et al. *Nucl. Instrum. Meth. A* 618(1):315 , 2010. doi:[10.1016/j.nima.2010.02.112](https://doi.org/10.1016/j.nima.2010.02.112)
64. HEMMER S.E. Study of Lepton Number Conserving and Non-Conserving Processes Using GERDA Phase I Data. Ph.D. thesis, Università degli Studi di Padova, 2014